

See discussions, stats, and author profiles for this publication at: <https://www.researchgate.net/publication/262912490>

A Data-Driven Stochastic Approach for Unmixing Hyperspectral Imagery

Article in IEEE Journal of Selected Topics in Applied Earth Observations and Remote Sensing · May 2014

DOI: 10.1109/JSTARS.2014.2328597

CITATIONS

8

READS

97

3 authors:



Jignesh S. Bhatt

Indian Institute of Information Technology, Vadodara

4 PUBLICATIONS 11 CITATIONS

[SEE PROFILE](#)



Manjunath V. Joshi

Dhirubhai Ambani Institute of Information and Communication Technology

79 PUBLICATIONS 837 CITATIONS

[SEE PROFILE](#)



Mehul S Raval

Ahmedabad University

69 PUBLICATIONS 259 CITATIONS

[SEE PROFILE](#)

Some of the authors of this publication are also working on these related projects:



Description based person identification in unconstrained surveillance video (2016 - 2019) [View project](#)



Session Title: Computational Intelligence for Digital Data Hiding (CIDDH) [View project](#)

A Data-driven Stochastic Approach for Unmixing Hyperspectral Imagery

Jignesh S. Bhatt, *Student Member, IEEE*, Manjunath V. Joshi, *Member, IEEE*, Mehul S. Raval, *Senior Member, IEEE*

Abstract

In this paper, we propose a two-step Bayesian approach to handle the ill-posed nature of the unmixing problem for accurately estimating the abundances. We use the fact that the abundances are dependent on the scene-contents and they represent mixing proportions of the endmembers over an area. In this work a linear mixing model is used for the image formation process in order to derive the data term. In the first step, a Huber-Markov random field (HMRF) based prior distribution is assumed to model the dependencies within the abundances across the *spectral space* of the data. The threshold used in the HMRF prior is derived from an initial estimate of abundances obtained using the matched filters. This makes the HMRF prior data dependent or data-driven and it helps in better handling of the ill-posedness. Final abundance maps are obtained in the second step within an *maximum a posteriori* (MAP) framework in which the prior term has data-driven HMRF (*dHMRF*). The resultant objective function is optimized using the particle swarm optimization (PSO) that ensures the global convergence. Theoretical analysis is carried out to show the effectiveness of the proposed method. The approach is qualitatively and quantitatively evaluated using the synthetic as well as real AVIRIS Cuprite data. The proposed method has the following advantages: 1) The estimated abundances are resistant to noise since they are based on an initial estimate that has high signal-to-noise ratio (SNR). 2) The variance in the abundance maps is well preserved since the threshold in the *dHMRF* is derived from the data itself.

Index Terms

Abundance estimation, Dirichlet process, Huber function, hyperspectral imaging, ill-posed problem, Markov random field (MRF), matched filter, particle swarm optimization (PSO), spectral unmixing.

I. INTRODUCTION

IMAGING spectroscopy of the earth has enabled quantitative analysis of an area within an instantaneous field-of-view (IFOV) of the sensor [1]. The hyperspectral imagers offer relatively large IFOV ($> 10m$ spot) and much finer ($10nm$ within more than 200 wavelength bands) spectral resolution. The higher spectral resolution enables the mixture analysis of contents in an area. The spectral unmixing of hyperspectral data has an ambitious objective to generate the abundance maps of various materials [2] found at different inaccessible areas of the earth. According to the linear mixing model (LMM) [3] of the hyperspectral data, the abundances are fractions of areas covered by the endmembers representing the pure spectra found in the data. Since the LMM provides a simple and mathematically tractable framework for solving the spectral unmixing problem, its use is prevalent among the research community working in the area of remote sensing. The linear stochastic mixing model (SMM) [4] for the hyperspectral data has been developed by integrating the principles of spectral clustering with the LMM, and its convergence issues are discussed in [5]. The SMM is also a kind of linear model since it assumes that the data is linear combinations of the endmembers, however, it considers the data in statistical manner by modeling the signatures in probabilistic sense rather than as deterministic spectra as in LMM. Though SMM offers the generalization, it has to handle an additional challenge of estimating the model parameters while solving for the spectral unmixing [6]. Over the past three decades, various geometrical, statistical and sparse-regression based endmembers identification and unmixing approaches have been investigated [7]. It has been recommended to explore random-field modeling to solve the problem and to develop the algorithms integrating the spatial and spectral information of the hyperspectral data [7]–[9]. The efficacy of the spectral unmixing can be assessed by checking the error between the ground or the available reflectance and the reflectance reconstructed using the estimated unmixed components. This requires accurate estimation of endmembers as well as the abundances at each location of the remotely acquired scene.

In spectral unmixing process, the number of endmembers is either known *a priori* or it can be determined using the state-of-art algorithm such as virtual dimensionality (VD) [10]. The endmembers are available in the spectral library [11] or they can be estimated from the data using various algorithms [7]–[9]. These algorithms are based on the convexity of the data and use the spectral space as in pixel purity index (PPI) [12], the N-FINDR [13], vertex component analysis (VCA) [14] and random PPI [15]. Few of them use spatial correlatedness within the band images in conjunction with the spectral measurements as in automatic morphological endmember extraction (AMEE) [16], spatial spectral endmember extraction (SSEE) [17], spatial preprocessing (SPP) [18] and spatial-spectral preprocessing (SSP) [19]. Knowing the endmember matrix, the given data can

Jignesh S. Bhatt (email: bhattjs@gmail.com, jignesh_bhatt@daiict.ac.in) and Manjunath V. Joshi (email: mv_joshi@daiict.ac.in) are with Dhirubhai Ambani - Institute of Information and Communication Technology (DA-ICT), Gandhinagar - 382007, India. Mehul S. Raval (email: mehul.raval@ahduni.edu.in) is with Institute of Information and Communication Technology (IICT), Ahmedabad University, Ahmedabad - 380009, India.

Manuscript received

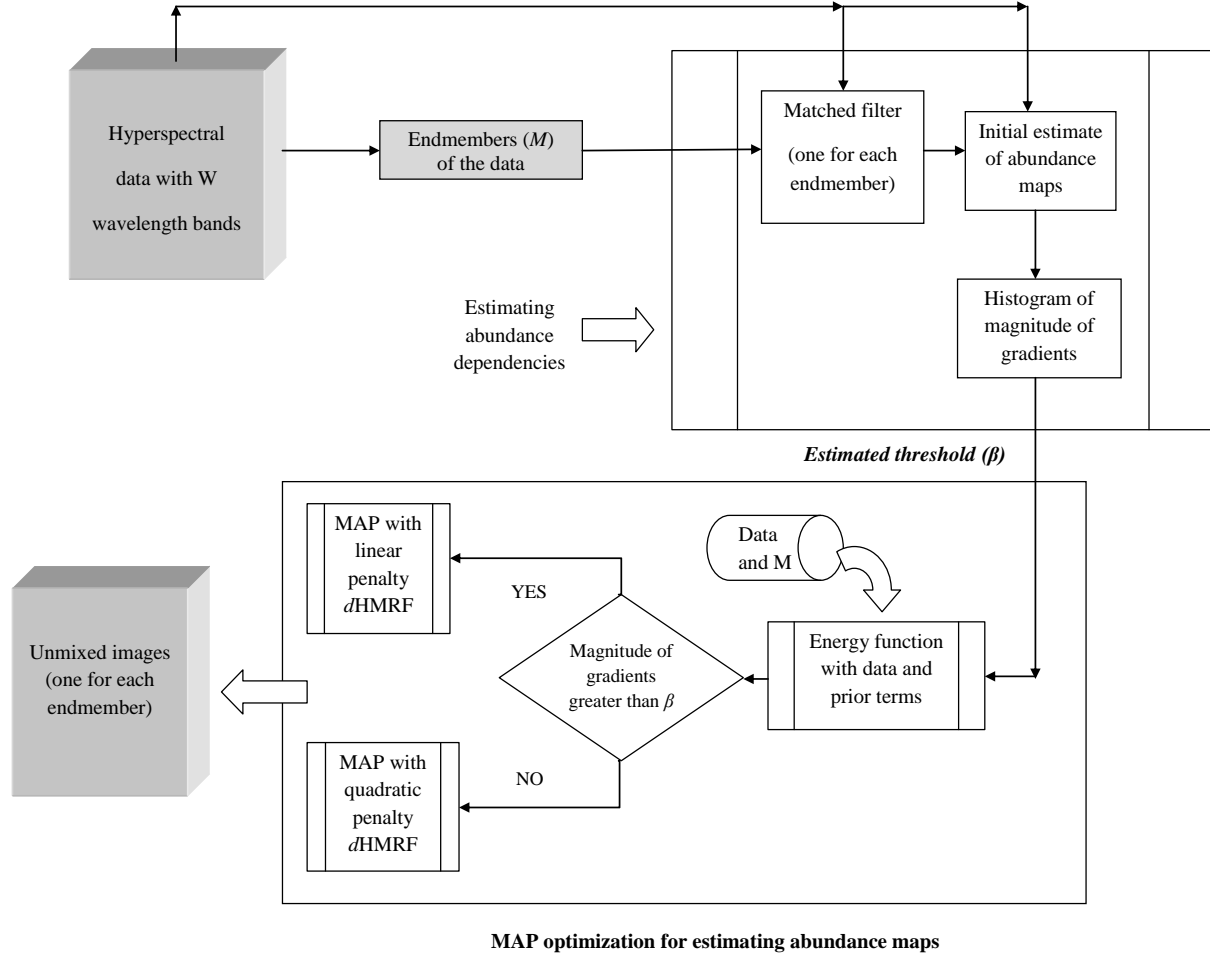


Fig. 1. Block schematic of the proposed MAP-dHMRF approach.

be unmixed by finding the corresponding abundances at each location over the scene. Since the abundances represent the endmembers fractions, they are constrained by nonnegativity as well as sum-to-one at each location.

The unmixing approaches can be broadly categorized into constraint-energy-minimization (CEM) [20], unconstrained regularization [21], maximum-likelihood (ML) [22], stochastic expectation maximization (SEM) [23], and neural network based approaches such as [24]. Majority of the research on abundance estimation is based on the ML estimation [25], [26]. Among the other approaches, fully constrained least-squares (FCLS) abundance estimation [27] is a well-known approach that represents generalization of the least-squares formulation. The methods based on the SMM are discussed in [4], [5]. In [28], a modified SEM is proposed for enhancing the unmixing performance. Authors in [29], [30] proposed unmixing based on total least squares (TLS) approach that restricts the solution to physically constrained abundances. In our recent work [31], we proposed a Tikhonov regularization based approach formulated in the TLS framework. A nonnegative solution using the principles of maximum entropy has been proposed in [32], [33] and [34]. In [35]–[39] the approaches based on Markov chain Monte Carlo method have been investigated. In addition to the nonnegativity, these methods also incorporate the sum-to-one constraint on the solution but they suffer from high computational complexity. Many of the methods proposed in the literature use different kind of priors for modeling the spatial correlation of the abundances [40]–[42]. These approaches consider every band independently without considering dependencies across the spectral space. Recently, we proposed a MAP-HMRF model based approach by considering Huber prior for the abundances over the spectral space [43] wherein a suitable value of manually selected threshold controls the solution.

A region in a scene has different proportions of mixing depending upon the amount of the constituent materials. Further, a pixel in the hyperspectral data represents reflectance spectra acquired from a large area (typically one pixel represents $20m \times 20m$) and hence it invariably forms mixed pixel at almost every location in the scene. The mixing proportions (i.e., abundances) vary at each location and the challenge is to capture these variations under the noisy conditions. Hence there is a need to individually unmix each location in order to obtain better estimate of abundance maps. The unmixing carried out

at every location across the scene preserves correlatedness of the abundances both spatially and spectrally. It may also be treated as special instance of the piecewise processing of data mentioned in [7]. This has motivated us to model the abundance dependencies at each location as Huber-MRF across the spectral range of the data. Depending on the chosen threshold, Huber function [44] simultaneously preserves smoothness and discontinuity within the abundances across the spectral space.

While solving the problem using the MAP-HMRF, we observe that the accurate estimation of abundances depends on the value of the Huber-MRF threshold. In [43] this threshold was chosen on a trial and error basis. Better way to find the Huber threshold is by using the true abundances, but these are unknown and are to be estimated. In order to estimate the threshold, one may consider using the learning based approach which requires a large hyperspectral data set. Hence deriving an accurate threshold using the training data set is computationally intensive. Moreover, one cannot generalize the use of such learned threshold for representing the dependencies of the abundances in any data. Since the abundances to be estimated are dependent on the given data, it is desirable to estimate the threshold using the available data itself, which can be used in the HMRF prior to achieve an accurate estimation of abundances.

Building on our previous work, in this paper, we automate the process of threshold selection based on an initial estimate of abundances obtained using the available data. Hence the resultant prior d HMRF now depends on the data, yielding accurate abundances. By estimating the threshold from the data, we avoid its empirical selection as done in our previous work [43]. A matched filter [45]–[48] based approach, inspired from the signal processing and communication theory is employed to obtain the initial estimate of abundances. The abundances derived using the matched filters act as a good approximation to represent the global characteristics of the true abundances. Hence, they can be used in obtaining the required threshold which in turn leads to improvement in the accuracy of estimated abundances. Thus the proposed approach obviates the training data resources to derive the threshold and gives abundances which minimize the data reconstruction error. In practice, the regularization parameter may be estimated by using generalized cross validation techniques [49]. However, this is computationally expensive and also the derived parameter is image dependent. Instead the use of proposed d HMRF prior helps in fixing the regularization parameter that further reduces the time complexity.

Considering the research in the spectral unmixing problem, we observe that the abundance estimation is relatively less focused when compared to the extraction of endmembers. Efforts have been made to incorporate the physical constraints (i.e., nonnegativity and sum-to-one) while estimating the abundances. However, the presence of noise and outliers make the unmixing process into severely ill-posed and hence it becomes difficult to obtain a unique solution. Many approaches estimate the abundances considering the spatial correlatedness but the variations of the abundance values across the spectral bands are not addressed. We explore the fact that the hyperspectral data is acquired over narrow and contiguous bands, which makes it spectrally correlated. The proposed *data-dependent* abundance prior over the spectral range of the data takes care of preserving the sudden variations as well as homogeneity in the abundances.

Accurate estimation of abundances is important for many applications in hyperspectral remote sensing. Few of these applications include hyperspectral image classification [50], content-based image retrieval system [51], [52], target detection [53], precision agriculture [54] and image fusion [55]. An accurate estimate of the abundance leads to better outcome in these applications. On the other hand, accurate abundances also lead to improved endmembers, since together they yield a pixel value (reflectance) in the data. As a matter of fact, in [56] the abundances have been used in finding the endmembers.

Considering the above mentioned reasons, we present a stochastic regularization based approach for estimating the abundance maps by making use of matched-filters and *data-driven* Huber-MRF (called as d HMRF). The formulated energy function is optimized using the PSO and in order to speed-up the convergence, the PSO is initialized with the different abundance particles estimated using various approaches. These include the FCLS [27] method, the estimate obtained by using the matched-filters based approach as well as the random particles derived from Dirichlet distribution [57]. We provide theoretical analysis of the proposed approach to illustrate how it improves the solution to overcome the ill-posedness in unmixing. In addition to the experimental validation using synthetic and real data, the choice of parameters is demonstrated and their sensitivity to the solution is also discussed.

Fig. 1 shows the complete block schematic of the proposed method. Given the hyperspectral data and the number of endmembers (e), we use the spectral library of the data to construct the endmember matrix (M). We then employ matched filters, one for each endmember and obtain initial estimates of the abundance maps. The abundance map has the same size as the available hyperspectral image and the number of abundance maps equals the number of endmembers. For example, a data cube of 224 bands each of size 75×75 pixels and having three endmembers has three abundance maps each of size 75×75 pixels. Once the initial estimate is available, it is used to derive the histogram of magnitude of gradients of these estimates using the gradients at every location. This histogram indicates the variations among the abundances. A suitable value of threshold β for Huber-MRF is then derived from this histogram, and is used for regularizing the solution. An energy function formed using the data term and the d HMRF prior with the estimated β is minimized to obtain the final solution.

The rest of the paper is organized as follows. Section II presents the hyperspectral image formation model. In section III we discuss the prior model. The approach for finding the Huber threshold from the initial estimate of abundance maps is dealt in section IV. Section V discusses the formulation of final energy function using the MAP- d HMRF and its optimization by PSO. In section VI we provide the theoretical analysis using geometric illustration to show the effectiveness of the proposed MAP solution. Section VII validates the performance of the proposed method with the experiments conducted on the synthetically

generated scene as well as on the real AVIRIS Cuprite scene data. Finally, section VIII concludes the paper.

II. HYPERSPECTRAL IMAGE FORMATION MODEL

The hyperspectral imager acquires hundreds of contiguous spectral measurements of an area. The data can be modeled as either linear or nonlinear mixing of the spectral signatures of various materials found in the area. We consider a linear mixing model at each location under the additive white Gaussian noise scenario as

$$\mathbf{r} = \mathbf{M}\boldsymbol{\alpha} + \mathbf{n}, \quad (1)$$

where the spectral measurement \mathbf{r} and the noise \mathbf{n} are W -dimensional column vectors with W indicating the number of available contiguous bands. Here, the endmember matrix \mathbf{M} representing the spectral signatures and it has size of $W \times e$, with e being the number of endmember vectors. The weights of these endmembers correspond to the abundances and they are denoted as a e -dimensional vector $\boldsymbol{\alpha} = [\alpha_1, \alpha_2, \dots, \alpha_e]^T$ where, α_i represents the fractional area covered by the i^{th} endmember, for $i = 1, 2, \dots, e$.

In the linear model given by equation (1) both \mathbf{M} and $\boldsymbol{\alpha}$ are unknown. In the proposed work, the \mathbf{M} is constructed using the ground truth spectral signatures and hence the problem returns to estimating the abundance maps, given both the \mathbf{M} and \mathbf{r} . In practice the number of endmembers (e) are significantly less than the available bands (W) for an acquired area of interest. Hence the equation (1) is overdetermined in $\boldsymbol{\alpha}$ making it an ill-posed inverse problem that requires regularization using suitable prior in order to make it a better-posed one. In the equation (1), \mathbf{n} represents independent and identically distributed (IID) noise having the joint probability density function (pdf) at a location (across the spectral cube) as

$$\mathbf{P}_r(\mathbf{n}) = \frac{1}{(2\pi\sigma^2)^{\frac{W}{2}}} \exp\left(\frac{-\|\mathbf{n}\|^2}{2\sigma^2}\right), \quad (2)$$

where σ^2 represents the noise variance.

III. PRIOR MODEL

Since we cast the problem in the MAP framework, a suitable prior is required in order to obtain a better solution. The prior has to take care of smoothness (slow variations) as well as discontinuity (sudden variations) of the abundance values. This can be done by choosing a prior that considers dependencies or correlatedness among the abundances. Markov random field (MRF) based model can effectively represent such dependencies. When an abundance map is modeled as an MRF, the abundance values at each location can be expressed as a joint pdf as

$$\mathbf{P}_r(\boldsymbol{\alpha}) = \frac{1}{Z} \exp\left(-\lambda \sum_{\mathbf{w}} \rho(\boldsymbol{\alpha})\right). \quad (3)$$

Note that equation (3) represents an MRF modeling the correlatedness among the abundances at a location. Here Z is the normalization constant that ensures total probability sum to unity and λ is a regularization (weighting) parameter, with $\rho(\boldsymbol{\alpha})$ representing the clique potential. The advantage of using MRF is that it represents a general model for quantifying correlatedness (dependencies) in the abundance values. One has the freedom to choose an appropriate clique potential in order to capture the dependencies in a better way. For an entity x modeled as an MRF, Huber has proposed the following clique potential [44],

$$\rho(x) = \begin{cases} x^2 & \text{if } x \leq \beta, \\ 2|x|\beta - \beta^2 & \text{if } x > \beta. \end{cases} \quad (4)$$

Here β denotes a constant called the Huber threshold. It can be seen from the equation (4) that depending upon the value of β the Huber-MRF can provide quadratic or linear penalty. By considering ρ as function of finite differences in $\boldsymbol{\alpha}$ at a location, i.e., $\alpha_d = |\alpha_i - \alpha_{(i+1 \bmod e)}|$, for $i = 0, 1, 2, \dots, e-1$, one may write equation (4) as

$$\rho(\alpha_d) = \begin{cases} \alpha_d^2 & \text{if } \alpha_d \leq \beta, \\ 2|\alpha_d|\beta - \beta^2 & \text{if } \alpha_d > \beta. \end{cases} \quad (5)$$

Note that if the $\alpha_d \leq \beta$ the smoothness in $\boldsymbol{\alpha}$ is preserved and $\alpha_d > \beta$ indicates that there exists significant difference (discontinuity) among the abundances. Hence, a proper choice of β is required in order to better preserve the gradual as well as sudden variations among the estimated abundances. In the next section, we discuss a method for extracting the β directly from the data based on the histogram of the initial estimate of abundances.

IV. DERIVING DATA-DEPENDENT THRESHOLD β

In the area of signal processing and communication theory, a matched filter is defined as a filter with an impulse response $h(t)$ that maximizes the output signal-to-noise ratio (SNR) for the given input signal $f(t)$ and is given by

$$h(t) = kf(t_0 - t), \quad (6)$$

where k is a constant and $f(t_0 - t)$ represents the input signal delayed by time t_0 .

When using hyperspectral data, the matched filter for a given endmember matrix is defined as [58]

$$\mathbf{MF}_i = \frac{\Sigma^{-1}(\mathbf{m}_i - \bar{\mathbf{R}})}{(\mathbf{m}_i - \bar{\mathbf{R}})^T \Sigma^{-1}(\mathbf{m}_i - \bar{\mathbf{R}})}, \text{ for } i = 1, 2, \dots, e, \quad (7)$$

where, \mathbf{MF}_i stands for a W -dimensional matched filter vector for the i^{th} endmember and the corresponding signature \mathbf{m}_i of size $W \times 1$. Here $\bar{\mathbf{R}}$ and Σ represent the sample mean vector and the covariance matrix of size $W \times 1$ and $W \times W$, respectively. Projecting the mean-subtracted endmember signature on the inverse of the data covariance Σ^{-1} indicates how well the endmember signature is correlated with the data. Matched filter output is then obtained by dividing the resultant product with the Mahalanobis distance [59] between the projected endmember signature and the data. Normalized \mathbf{MF}_i indicates the contribution of i^{th} endmember signature in the data.

Now using equation (7), one can obtain the initial estimate of the corresponding abundance $\hat{\alpha}_{init_i}$ as

$$\hat{\alpha}_{init_i} = \langle \mathbf{r} - \bar{\mathbf{R}}, \mathbf{MF}_i \rangle, \text{ for } i = 1, 2, \dots, e, \quad (8)$$

where, $\langle \cdot, \cdot \rangle$ represents the inner product. Here $\hat{\alpha}_{init_i}$ gives the initial estimate of the abundance of the i^{th} endmember. The equation (8) is applied at every pixel vector of the data cube for all available endmembers, which yields e number of initial abundance maps each of size $\mathbf{N}_1 \times \mathbf{N}_2$ pixels.

The initial estimate of abundances using equation (7) and equation (8) may not correspond to the abundances closer to their true values. This is because although the abundances estimated using the equations (7) and (8) make use of the data covariance in order to enhance the output SNR of endmembers, they do not correspond to optimal unmixing [58]. However they serve as better estimate in finding the required parameters that indicate the global dependencies of abundances. Hence, we use the matched filters to find the initial estimate of abundances as given by equation (7). This in turn is employed in estimating the threshold (β). Following steps are used in finding the threshold β :

- 1) Using the available initial estimate of abundances, calculate the magnitude of gradient at each location. This yields a gradient cube of size $\mathbf{N}_1 \times \mathbf{N}_2 \times e$.
- 2) Find the histogram for the magnitude of gradients obtained in step 1.
- 3) Locate the densely populated gradient bins located near the tail of the histogram. This region represents higher probability of noncoherence among the abundance values.
- 4) Select the center of the bins in step 3 as the threshold β .

Since the derived value of β now depends on the data, we call this HMRF as d HMRF i.e., data-dependent HMRF.

V. MAP- d HMRF BASED UNMIXING

In order to solve the problem using the MAP estimation, we need to maximize the probability of α given the data, i.e., maximize $\mathbf{P}_r(\alpha | \mathbf{r})$, $\forall \alpha$. Using the Bayes' rule one may write MAP estimate of α as

$$\hat{\alpha} = \arg \max_{\alpha} \mathbf{P}_r(\mathbf{r} | \alpha) \mathbf{P}_r(\alpha) \quad (9)$$

$$\text{s.t.}: 0 \leq \hat{\alpha}_i \leq 1, \forall i \text{ and } \sum_{i=1}^e \hat{\alpha}_i = 1.$$

Since maximizing the probabilities in the equation (9) is equivalent to maximizing their logarithmic probabilities, the equation (9) can now be written as

$$\begin{aligned} \hat{\alpha} &= \arg \max_{\alpha} [\log P_r(\mathbf{r} | \alpha) + \log P_r(\alpha)] \\ &= \arg \min_{\alpha} [-\log P_r(\mathbf{r} | \alpha) - \log P_r(\alpha)]. \end{aligned} \quad (10)$$

Here the first and the second terms represent the likelihood probability and the prior probability, respectively. Using the equations (1) and (2) one can show that the likelihood probability at every location can be obtained as

$$\mathbf{P}_r(\mathbf{r} | \alpha) = \frac{1}{(2\pi\sigma^2)^{\frac{W}{2}}} \exp\left(-\frac{\|\mathbf{r} - \mathbf{M}\alpha\|^2}{2\sigma^2}\right). \quad (11)$$

Using the equations (3), (5), (10) and (11) one can obtain the estimate of abundances ($\hat{\alpha}$) as the minimization of the following energy functions,

$$\hat{\alpha} = \begin{cases} \arg \min_{\alpha} \left[\frac{\|\mathbf{r} - \mathbf{M}\alpha\|^2}{2\sigma^2} + \lambda \sum_{i=0}^{e-1} |\alpha_i - \alpha_{(i+1 \bmod e)}|^2 \right], & \text{if } \alpha_d \leq \beta, \\ \arg \min_{\alpha} \left[\frac{\|\mathbf{r} - \mathbf{M}\alpha\|^2}{2\sigma^2} + \lambda \sum_{i=0}^{e-1} (2|\alpha_i - \alpha_{(i+1 \bmod e)}| \beta - \beta^2) \right], & \text{if } \alpha_d > \beta. \end{cases} \quad (12a)$$

The first term in each of these equations represents the data-term and the second term represents the prior-term. Here λ indicates the weighing factor between these two terms. The incorporation of the d HMRF as the prior distribution on the abundance maps allows us to simultaneously preserve the smoothness and sudden variations among the abundances. This is because the quadratic penalty $\alpha_d \leq \beta$ in equation (12a) preserves the smooth variations while the discontinuities in the abundances are taken care by the linear penalty for $\alpha_d > \beta$ by equation (12b). The equations (12a) and (12b) simultaneously minimized making use of a global optimization technique particle swarm optimization (PSO) [60]. Though the PSO is an evolutionary approach, it has a simple implementation structure. Recently, PSO has been successfully used as an optimization tool in solving various problems related to the hyperspectral data, such as precise recovery of the endmembers [61], and better classification of hyperspectral data [62]. It can also be implemented in parallel form in order to reduce the time complexity.

A key to fast convergence of PSO lies in its initialization with problem-specific group of particles. In this work, we use a group of initial particles derived from Dirichlet density function that ensures nonnegativity and the sum-to-one constraints on the abundance values. Dirichlet function has been used in the spectral unmixing for detecting endmembers and in modeling the abundances [63]–[65]. The other particles in the optimization include the abundances estimated using the FCLS [27] method and the initial abundance maps obtained from our matched-filters approach.

The PSO searches for the best solution through an iterative process by computing the fitness cost. Let α_{bp}^k and α_{bg}^k be the personal and the global best particles, respectively, at the k^{th} iteration with the fitness values $F_{\alpha_{bp}^k}$ and $F_{\alpha_{bg}^k}$, respectively. While optimizing using PSO, the velocity V_{α_b} and the position α_b (abundance value) are updated as,

$$V_{\alpha_b}^{k+1} = w\alpha_b^k + c_1r_1(F_{\alpha_{bp}^k} - F_{\alpha_b^k}) + c_2r_2(F_{\alpha_{bg}^k} - F_{\alpha_b^k}), \quad (13)$$

and

$$\alpha_b^{k+1} = \alpha_b^k + V_{\alpha_b}^k, \quad (14)$$

where r_1 and r_2 are random numbers with uniform distribution in $[0, 1]$. Here w , c_1 and c_2 are the constants representing the memory of previous velocities, cognitive and social parameters, respectively. The final values of α are obtained iteratively using the equations (13) and (14), respectively. The convergence is obtained when every particle has the same personal best that equals the global best. This minimization is carried out at each location in order to estimate the complete abundance maps.

VI. THEORETICAL ANALYSIS OF MAP- d HMRF BASED UNMIXING

We now carry out the theoretical analysis of the proposed approach and compare it with the FCLS [27] and MaxEnt [34] approaches. This analysis illustrates the effectiveness of the proposed approach for solving unmixing problem.

The remotely sensed hyperspectral reflectance is inevitably corrupted by the noise originating from various sources which can be conveniently modeled as additive white Gaussian noise (AWGN). Given the corrupted data \mathbf{r} acquired over the W contiguous bands and the endmember matrix \mathbf{M} , the linear unmixing estimates the underlying abundance values α of every endmember. Solving the unmixing problem using a mixing model as given in equation (1) is challenging due to the following reasons, 1) though the endmembers are linearly independent, they may be correlated yielding ill-conditioned endmember matrix. This causes errors while inverting it to obtain the abundances and makes the abundance estimation sensitive to the noise [7], 2) the measured data-vectors across the spectral bands are convex combinations of endmembers enforcing additional constraints on the abundances, i.e., they should be nonnegative and sum-to-one, at each pixel location, and 3) the presence of noise and outliers as well as the overdetermined system of equations makes it difficult to find the true α .

In order to carry out the analysis, let us consider the geometric representation of various vectors which can be shown using the nonzero line segments. The acquired data over different locations of the scene can be considered as vectors in the W -dimensional nonnegative real vector space, i.e., \mathbb{R}^{+W} . The endmembers are the set of linearly independent vectors (bases) that span the given data vector space. The abundances represent the weights of these basis vectors and their linear combinations form the data vectors in the \mathbb{R}^{+W} . The solution space of abundances and various vectors can be better illustrated by considering 2-D space with $W = 2$. Consequently two linearly independent vectors of the \mathbb{R}^{+2} representing the two endmembers \mathbf{m}_1 and \mathbf{m}_2 are depicted as $\overrightarrow{\mathbf{om}_1}$ and $\overrightarrow{\mathbf{om}_2}$ in Fig. 2 (a). One may express the LMM at a pixel location using the vector-matrix notation as follows,

$$\mathbf{r}_{\text{true}} = \begin{bmatrix} r_1 \\ r_2 \end{bmatrix} = \alpha_1 \begin{bmatrix} m_{11} \\ m_{21} \end{bmatrix} + \alpha_2 \begin{bmatrix} m_{12} \\ m_{22} \end{bmatrix}, \text{ where } \mathbf{m}_1 = \begin{bmatrix} m_{11} \\ m_{21} \end{bmatrix} \text{ and } \mathbf{m}_2 = \begin{bmatrix} m_{12} \\ m_{22} \end{bmatrix}, \text{ hence } \mathbf{M} = \begin{bmatrix} m_{11} & m_{12} \\ m_{21} & m_{22} \end{bmatrix}. \quad (15)$$

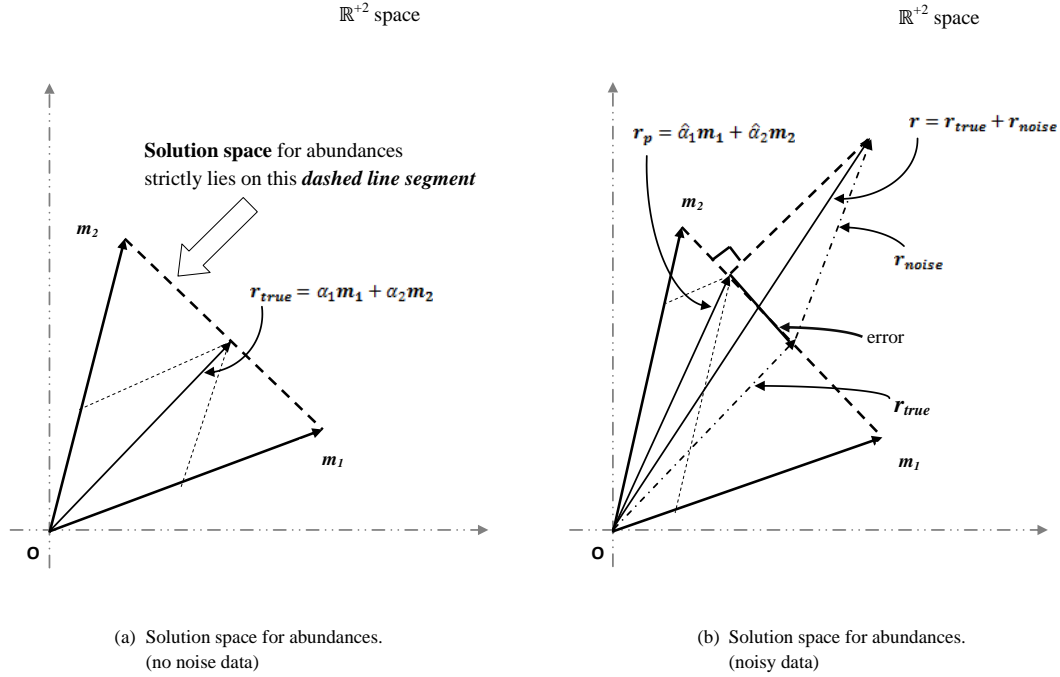


Fig. 2. A 2-D example to illustrate the solution space for abundances.

Here m_1 and m_2 represent the endmember vectors, and the scalars α_1 and α_2 their abundances at that location. As shown in equation (15), the vector r_{true} is a linear combination of the endmembers m_1 and m_2 with α_1 and α_2 as their weights. Since $\alpha_1 + \alpha_2 = 1$, the solution space (i.e., a line in the 2-D case) for α strictly lies on the dashed line segment as shown in Fig. 2 (a). It may be noted that Fig. 2 (a) represents an ideal scenario in which no noise is considered in the data, and the M and α correspond to their true values. Fig. 2 (b) shows the practical scenario in which the data is corrupted by the additive noise r_{noise} giving the measured reflectance as r instead of r_{true} , i.e.,

$$r = r_{true} + r_{noise} = \begin{bmatrix} r_1 \\ r_2 \end{bmatrix} + \begin{bmatrix} n_1 \\ n_2 \end{bmatrix}. \quad (16)$$

Using this r and M , we need to estimate the values of the abundances, i.e., $\hat{\alpha}_1$ and $\hat{\alpha}_2$, such that their linear combination with the m_1 and m_2 yields a projection vector r_p on the solution line shown as dashed. One can estimate the values of abundances such that the error $\|r_{true} - r_p\|^2$ is minimum, with the constraint that $\alpha_1 + \alpha_2 = 1$. A least-squares with a condition that the abundances sum-to-one can be solved as,

$$\arg \min_{\alpha} \|r - M\alpha\|^2 \text{ such that } \hat{\alpha}_1 + \hat{\alpha}_2 = 1. \quad (17)$$

Note that when the abundances are nonnegative, the equation (17) leads to the fully-constrained solution, i.e., FCLS solution. Fig. 2 (b) shows this projection, reconstructed vector r_p and the associated error. Since any point on the dashed line segment could be a candidate solution, the problem is ill-posed. Solving such a problem is difficult due to the presence of noise as well as outliers in the data. In practice, the number of endmembers is considerably less than the available bands (W) and the unmixing becomes a severely ill-posed problem. In such cases, one has to regularize the solution using prior information about the solution.

Let us consider the solutions obtained by using different approaches while solving the unmixing problem. The solutions obtained using the FCLS [27] method and MaxEnt [34] approach are optimum in the least-squares sense. The FCLS initializes with abundances obtained using nonnegatively constrained least-squares (NCLS) approach [66] and iteratively converges to the fully constrained solution. The MaxEnt initializes the solution with the uniform abundances using their entropy which inherently provides nonnegative constraint. Although this incorporates the physical constraints on the abundances, it also converges in the LS sense [34] and provides a comparable performance with the FCLS. As per the Bayesian principles under the condition of IID Gaussian noise, the LS solution is equivalent to the maximum-likelihood (ML) estimation. This is equivalent to solving the problem using MAP in which uniform distribution is assumed for the prior, i.e., we obtain the estimate as

$$\hat{\alpha} = \arg \max_{\alpha} P_r(\alpha|r) = \arg \max_{\alpha} P_r(r|\alpha) = \arg \min_{\alpha} \|r - M\alpha\|^2 \quad (18)$$

s.t.: $0 \leq \hat{\alpha}_i \leq 1$, for $i = 1, 2, \dots, e$. and $\sum_{i=1}^e \hat{\alpha}_i = 1$.

Equation (18) indicates that both the FCLS and MaxEnt assume uniform distribution for the prior yielding the LS solution. This also indicates that no assumption is made on the solution space which in turn increases the error while estimating the abundances. Unlike these approaches, the proposed approach uses the MAP framework that incorporates the data-dependent prior while solving for abundances. Our approach uses additional information about the variations in the abundances which is derived from the initial estimate and improves the constrained least-squares solution. As discussed in section IV, the initial estimate obtained using the matched-filters approach is based on the data covariance and hence the derived threshold β provides the required information about the abundances variations. Use of proper value of β in our MAP solution results in abundances that reduce the data reconstruction error.

The performance improvement of the proposed approach can now be analyzed using the geometric illustration. Continuing with the 2-D example, the given reflectance represents a mix of two endmembers with the proportions based on the area covered by these spectral signatures. Fig. 3 shows geometric representation of various vectors and the solutions using the FCLS, MaxEnt and the proposed methods. As shown in Fig. 3 (a), we consider two linearly independent endmember vectors \mathbf{m}_1 and \mathbf{m}_2 depicted as $\overrightarrow{0\mathbf{m}_1}$ and $\overrightarrow{0\mathbf{m}_2} \in \mathbb{R}^{+2}$. We know that the solution space for the abundances has to lie on the line segment $\overline{\mathbf{m}_1\mathbf{m}_2}$. Given the corrupted \mathbf{r} , one needs to find a projection of the \mathbf{r} on the line segment $\overline{\mathbf{m}_1\mathbf{m}_2}$ in order to locate the abundances.

Fig. 3 (a) shows the solution space for the proposed approach. Here, the optimization is carried out by using the PSO which we initialize the abundances using the particles drawn from Dirichlet distribution including those estimated using the other approaches and these are inherently nonnegative and sum-to-one. The resultant solution using the formulation given in equation (9) is guaranteed to lie within the physically acceptable range of abundances, i.e., they lie on the line segment $\overline{\mathbf{m}_1\mathbf{m}_2}$. Fig. 3 (a) shows different projections of \mathbf{r} on $\overline{\mathbf{m}_1\mathbf{m}_2}$ due to initialization by the candidate abundance particles.

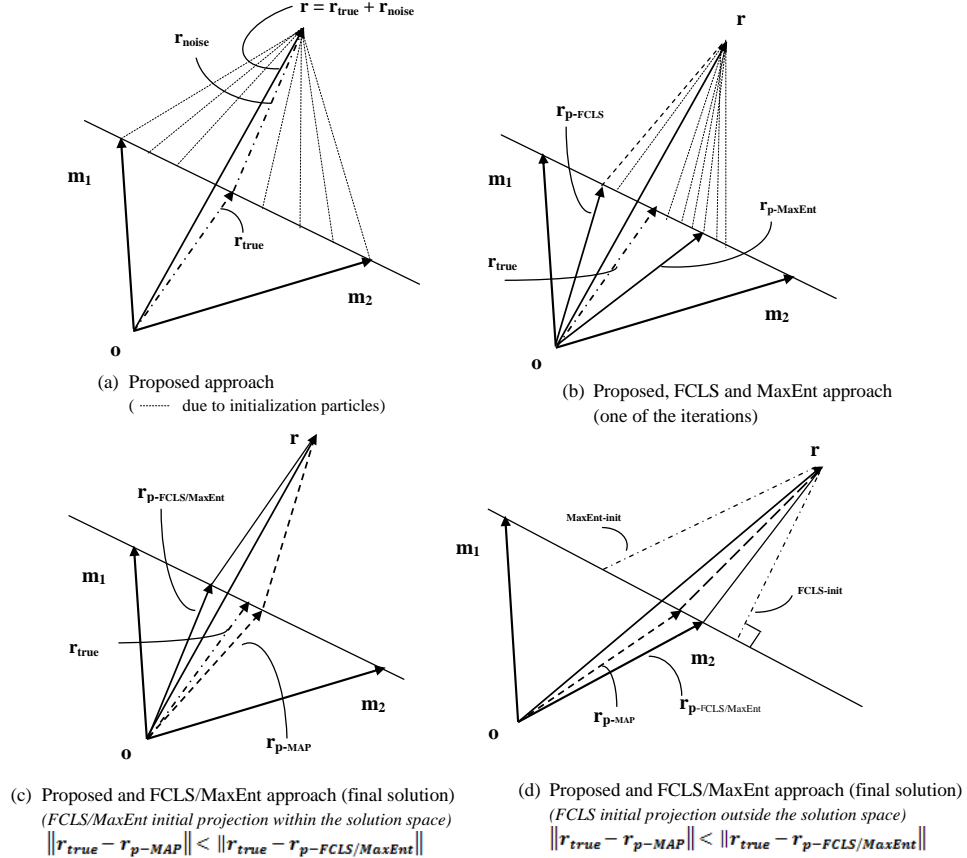


Fig. 3. Geometric illustration of the proposed MAP-dHMRF solution compared with the FCLS/MaxEnt solution.

Fig. 3 (b) depicts the scenario for one of the iterations for the three approaches. FCLS initializes with the abundances obtained using the NCLS [66] and the MaxEnt with uniform abundances. Both the FCLS and MaxEnt yield the mean squared error as $\|\mathbf{r} - \mathbf{M}\alpha_{FCLS/MaxEnt}\|^2$. The proposed approach performs the MAP optimization on the initial abundance particles iteratively then finally converges to the solution. Fig. 3 (b) shows that as the iterations progress, the initialized particles in our approach converge to a set of projection vectors that yield better abundances. Fig. 3 (c) depicts the final solution for the three methods. As seen from the Fig. 3 (c) we have $\|\mathbf{r}_{true} - \mathbf{r}_{p-MAP}\|_2 < \|\mathbf{r}_{true} - \mathbf{r}_{p-FCLS/MaxEnt}\|_2$. This is because the

TABLE I
A COMPARATIVE SUMMARY OF THE FCLS METHOD, THE MAXENT APPROACH AND THE PROPOSED MAP-*d*HMRP APPROACH.

Algorithm	Inputs	Initial estimate	Working principle	Ill-posedness*	Optimization	Initialization	Solution	Output
FCLS [27]	\mathbf{r} & \mathbf{M}	-	FCLS	-	Quadratic prog.	NCLS [66]	ML	constrained $\hat{\alpha}$
MaxEnt [34]	\mathbf{r} & \mathbf{M}	-	FCLS + entropy prior	-	Gradient descent	uniform $\hat{\alpha}$	ML	constrained $\hat{\alpha}$
proposed	\mathbf{r} & \mathbf{M}	matched-filters	FCLS + <i>d</i> HMRP prior	Yes	PSO	candidate $\hat{\alpha}$	MAP	constrained & improved $\hat{\alpha}$

*takes care of noise and outliers in \mathbf{r} , ill-conditioning of \mathbf{M} and sudden variations in abundances.

data-dependent HMRF prior forces the solution closer towards the true abundances α_1 and α_2 so the reconstructed reflectance is closer to \mathbf{r}_{true} . The β derived from the initial estimate of the abundances forces the minimization in equation (12) to the true solution by imposing the additional condition of dependencies of the abundances. This clearly indicates that the solution using the proposed approach represents better unmixing.

In order to show superiority of the proposed method even when a measured reflectance \mathbf{r} has the dominance of one of the endmembers, i.e., when we consider that the significant content of the scene is due to one of the materials, the situation is as shown in Fig. 3 (d). Note that in this case the abundance for \mathbf{m}_1 has a small nonzero value but the \mathbf{m}_2 dominates. For such a data, the initial error projection for FCLS is outside the limits of $\overline{\mathbf{m}_1\mathbf{m}_2}$ as shown by FCLS-init in Fig. 3 (d). Since the FCLS converges in the LS sense, at most it converges to a point where the reflectance vector is $\overline{\mathbf{0m}_2}$ and hence results in $\hat{\alpha}_1 = 0$ and the $\hat{\alpha}_2 = 1$ which are incorrect. This is because $\hat{\alpha}_1$ is small but nonzero. As shown in Fig. 3 (d), the MaxEnt initializes the abundances with the uniform distribution giving the initial error vector projection MaxEnt-init. Both the MaxEnt and the FCLS converge to the same solution which is shown as $\mathbf{r}_{\text{p-FCLS/MaxEnt}}$ in Fig. 3 (d). On the other hand, as already explained the proposed approach iteratively chooses the abundances and yields a projection that results in nonzero abundance value for $\hat{\alpha}_1$ and a value of $\hat{\alpha}_2$ closer to 1 thus reflecting the dominance by the \mathbf{m}_2 as required. This is shown by the projection $\mathbf{r}_{\text{p-MAP}}$ in Fig. 3 (d). Thus in our approach, we obtain better solution when compared to the FCLS as well as MaxEnt methods, even when one of the endmembers is dominant in the data.

Table I shows the comparative summary of various key features of the FCLS, MaxEnt and the proposed method. It is clear from the Table I that the proposed approach makes use of additional details about the entity to be estimated in order to improve the solution.

VII. EXPERIMENTAL ANALYSIS

We now demonstrate the efficacy of our regularization based approach to recover abundances from the given data. We first conduct the experiments on the synthesized images using three spectral signatures of the US Geological Survey (USGS) digital spectral library [11]. Next, we show the experiments on the real data collected by the Airborne Visible/InfraRed Imaging Spectrometer (AVIRIS) over the Cuprite mining site area [67]. Finally, we discuss the choice of various parameters used in the optimization and give the sensitivity analysis of the parameter λ and β .

The implementation of the algorithms are done in MATLAB[®] running on a 64-bit operating system. All the algorithms are run on a Desktop PC with Intel[®] Core[™] i5-3210M CPU at 2.5 GHz with 4 GB of RAM. We compare the performance of the proposed method with two of the state-of-art approaches, the FCLS [27] and the MaxEnt [34]. Comparison of the proposed approach is also done with the results obtained using our previous work [43]. Further we compare the results with Tikhonov regularization [31] which is based on the total least squares (TLS) formulation. We also demonstrate the unmixing results by imposing only the nonnegativity constraint in the proposed method and compare the performance with the nonnegative constrained least-squares (NCLS) [68] method. The various parameters used while minimizing the proposed energy function using PSO are tabulated in Table II. These parameters were fixed after verifying them for satisfactory results on synthetic data.

TABLE II
PARAMETERS USED IN THE PROPOSED MAP-*d*HMRP ENERGY FUNCTION.

Parameter	Value
w	0.01
c_1	0.01
c_2	0.01
λ	1.00

A. Experiments with synthetically generated data

For constructing the synthetic data, we use the 224 contiguous band reflectance spectra in the spectral range of 400-2500 nm. The data has three spectrally distinct materials namely, Ammonioalunite NMNH145596, Brucite HS247.3B and Andradite WS487 and are downloaded from the USGS library [11]. The signatures of these materials, i.e., endmember values, are known which form an endmember matrix \mathbf{M} of size 224×3 where the three column vectors correspond to the spectral signatures. Using the known abundance vector α of size 3×1 , a pixel vector \mathbf{r}_{true} is constructed as $\mathbf{r}_{\text{true}} = \mathbf{M}\alpha$, generating a 224×1

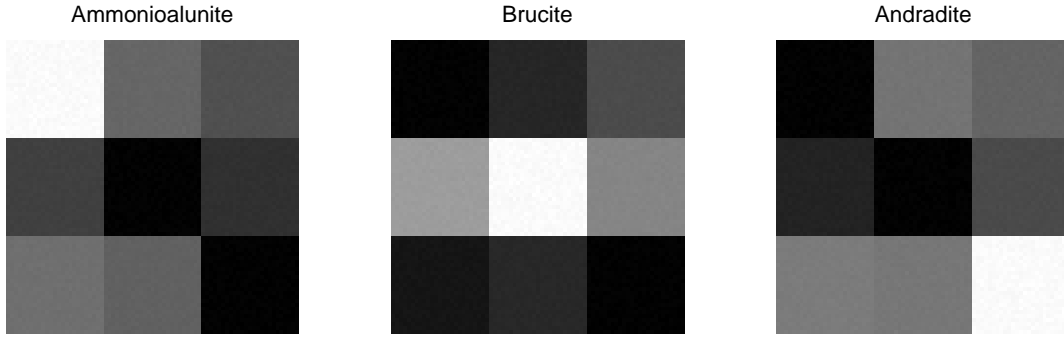


Fig. 4. Ground truth abundance maps for the three endmembers of synthetic data.

reflectance data vector. Considering an image of size 75×75 pixels for each band, a total of $75 \times 75 = 5625$ reflectance vectors are generated. This yields a 224-band hyperspectral ground truth reflectance cube with each band image having a size of 75×75 pixels. The corresponding ground truth abundance maps each of size 75×75 pixels are shown in Fig. 4. It can be seen that the scene is divided into nine regions with each region having different linear mixing proportions. This kind of mixing is chosen to test our algorithm on both homogeneous as well as heterogeneous nature of abundance values. The experiments are conducted to estimate the abundance maps for different levels of the additive noise in the reflectance, i.e., the synthesized data.

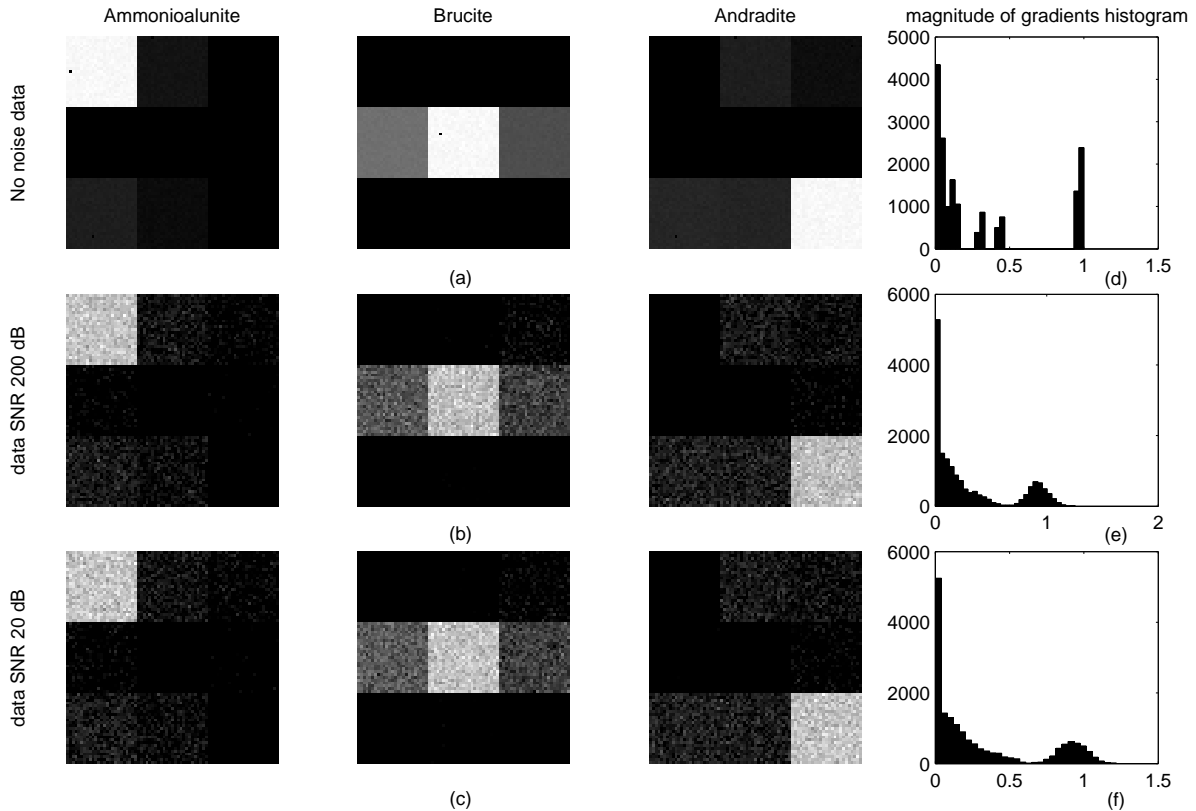


Fig. 5. Deriving data-dependent β from the synthetic data: Initial estimate of abundances (a) with no noise data, (b) with 200 dB SNR data, and (c) with 20 dB SNR data. The plots in (d), (e), and (f) are corresponding histograms of magnitude of gradients of abundances at each location.

We first derive Huber threshold β from the available data. The initial estimate of abundance maps are obtained using the matched filters approach as discussed in section IV as follows. Matched filter responses are obtained using equation (6) where the endmember matrix constructed using the USGS library signatures [11] are utilized. Then using the equation (7), the inner product of the filtered output and the mean subtracted data vector results in the initial estimate of the abundances. These estimates are used to obtain the histogram of the magnitudes of gradients from which the β value is derived. The initial estimates of abundance maps for increasing amounts of noise in the data are shown in Fig. 5. No noise case, i.e., $\text{SNR} = \infty$, is shown in Fig. 5 (a). In Fig. 5 (b) and Fig. 5 (c), we show these maps for 200 dB and 20 dB SNR, respectively. The histograms of magnitude of gradients of the estimated abundances computed for each case are displayed in Fig. 5 (d-f). Following the steps given in section IV, the values of β selected from the histograms are 0.20, 0.1927, and 0.18, for the three cases of no noise, SNR 200 dB and SNR 20 dB, respectively. These values of β are used in our MAP framework to obtain the final abundance maps. Note that the selected β correspond to the center of the gradients region that indicates the high probability of occurrence of discontinuities in abundances.

The abundance maps estimated by using the FCLS [27] and the MaxEnt [34] approaches for the case of 20 dB SNR are shown in Fig. 6 (a) and Fig. 6 (b), respectively. The final result of our approach using the β value selected from the proposed method is shown in Fig. 6 (c). It can be seen that the spatial variations of the abundances estimated using the proposed approach are consistent with the ground truth maps shown in Fig. 4 as well as when compared to the estimated maps shown in Fig. 6 (a) and Fig. 6 (b). We mention here, although the final results are shown for the case of lowest SNR only, the initial estimates of abundances are displayed for SNR of 200 dB as well as 20 dB. This is done in order to point out the resulting variations in estimated values of β . In order to illustrate how well the solution depends on the proper choice of β as done in

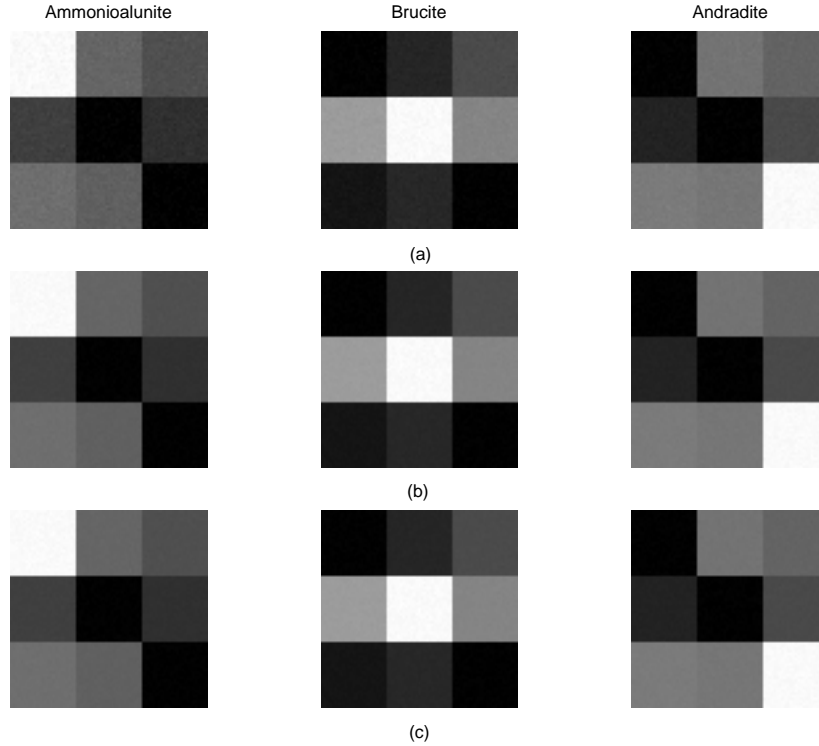


Fig. 6. Unmixed images for synthetically generated data with 20 dB SNR: Estimated abundance maps by using (a) the FCLS [27] method, (b) the MaxEnt [34] approach, and (c) the proposed MAP-dHMRf approach.

the proposed method, we show the plots of pixel locations Vs. estimated abundance values for selected regions considering the low and high variations of abundances. Fig. 7 (a), Fig. 7 (b), and Fig. 7 (c) display the abundance maps of Ammonioalunite, Brucite and Andradite, respectively, with a heterogeneous and a homogeneous region in the data marked as rectangles with red and yellow borders, respectively. These selected regions are also marked in the mean image of the 224 contiguous band synthetic data in Fig. 7 (d). The corresponding pixel locations within the regions Vs. abundance values are shown separately for each material in Fig. 8. Plots in Fig. 8 (a) show abundances for a heterogeneous region while Fig. 8 (b) display abundances for a homogeneous region. In each plot we show abundances estimated using the FCLS method and the proposed approach for $\text{SNR} = 20$ dB. The ground truths are also shown for the comparison. As expected, one can see from the figure that the estimated abundances at different locations using the proposed approach are closer to the ground truth. This indicates that the

proper choice of β is important for better estimates of abundances. Here, we avoid showing the comparison with the MaxEnt approach since it has comparable performance to the FCLS method.

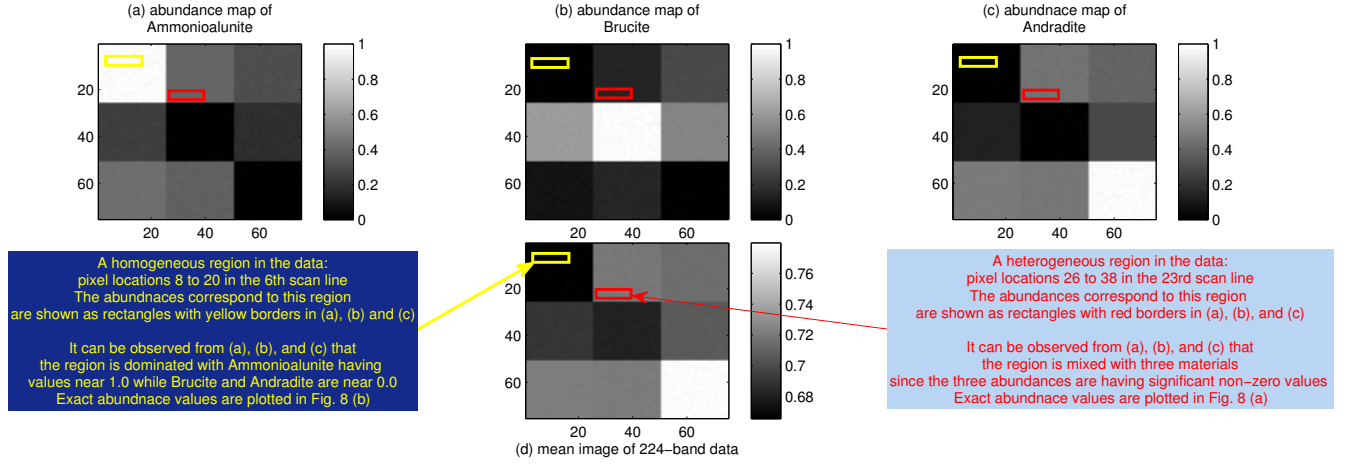


Fig. 7. Selected regions shown in the abundance maps and in the mean image of 224 contiguous bands synthetically generated data. Abundance map of (a) Ammonioalunite, (b) Brucite, and (c) Andradite, with a heterogeneous and a homogeneous regions in the data marked as rectangles with red and yellow borders, respectively, and (d) mean image of the 224-band data with the corresponding regions marked with the rectangles using the respective colors. The corresponding abundance values for the heterogeneous and the homogeneous regions are shown in Fig. 8 (a) and in Fig. 8 (b), respectively.

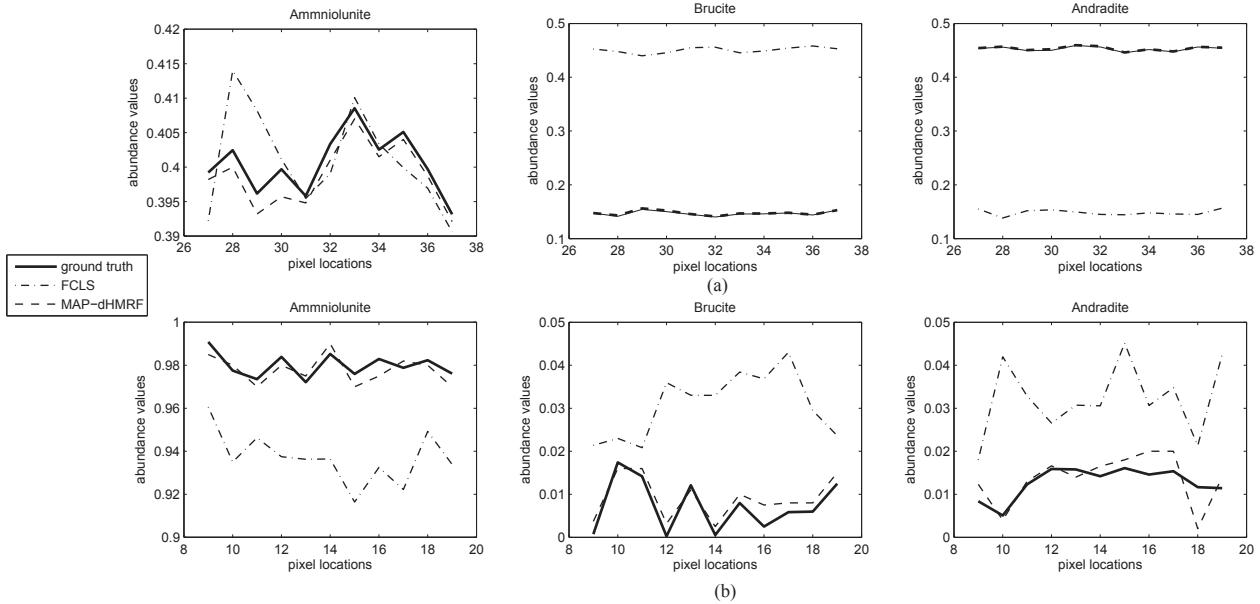


Fig. 8. Pixel locations Vs. estimated abundances on selected regions within synthetic data (20 dB SNR): (a) estimated abundances in the heterogeneous reflectance region (a region where abundance values are almost similar referring to rectangles with red borders in Fig. 7) using FCLS method [27] and using the proposed approach, and (b) estimated abundances in the homogeneous reflectance region (a region where abundance values have discontinuity referring to rectangles with yellow borders in Fig. 7) using FCLS method [27] and using proposed approach. Note that the scale in the graphs of (a) and (b) are different, indicating higher variance in the abundances displayed in (b).

We now discuss the quantitative performance of the proposed approach and compare the same with the other approaches. In order to do this, we used the following measures: root mean squared error (RMSE) [69], spectral angle mapper (SAM) [70] and spectral information divergence (SID) [71]. These measures are considered in order to assess the preservation of the spatial as well as spectral characteristics in the estimated abundances. Lower values of the RMSE ensures the spatial fidelity while lower values of the SAM and SID indicate the spectral fidelity. These measures averaged over the entire set of abundance values i.e., $75 \times 75 \times 3$ are shown in the Table III for various approaches. These values shown under NSCA (nonnegative and sum-to-one constrained abundances) in the table indicate the performance for increasing levels of noise in the data starting from 1000 dB to 20 dB SNR. From the Table III we observe that as far as the performance in terms of quantitative measures are concerned, the proposed approach outperforms all the other approaches, with the exception of FCLS performing little bit better in terms

of RMSE at high SNR of 1000 dB. The reasons for this are as follows. The noise in the data is almost non-existent at such a high SNR making it free from outliers, so the FCLS method being the least-squares approach converges to a solution that yields abundances closer to the true values. However, the proposed approach uses the prior information in terms of d HMRF and hence forces the solution to drift relatively from the true abundances even when the noise level in the data is minimum. One can see that even though FCLS has better spatial fidelity at low noise level, it performs poor in terms of preservation of spectral characterization which is clearly evident from the high values for SAM and SID. One may conclude that at lower noise level, the proposed MAP- d HMRF approach exhibits spatial enhancement comparable to the state-of-art method such as FCLS approach but it performs better as far as spectral preservation is concerned. It should be noted that for increasing levels of noise, the proposed approach outperforms all the other approaches.

TABLE III
NOISE SENSITIVITY ANALYSIS AND COMPARATIVE PERFORMANCE.
AVERAGE ERROR SCORES FOR THE UNMIXING WITH THE SYNTHETIC DATA
THE MINIMUM VALUES OF EACH ERROR ARE SHOWN IN BOLD TYPEFACE

Measure	Abundances	Algorithm	SNR = 1000 dB	SNR = 200 dB	SNR = 50 dB	SNR = 20 dB
RMSE [69]	NSCA	FCLS [27]	0.0005	0.0088	0.0102	0.0177
		MaxEnt [34]	0.0896	0.1836	0.2638	0.2740
		TLS-Tikhonov [31]	0.0436	0.1014	0.2533	0.2681
		MAP-HMRF [43]	0.0785	0.1237	0.2733	0.2783
		proposed (MAP- d HMRF)	0.0008	0.0012	0.0022	0.0025
	NCA	NCLS [68]	0.0004	0.0093	0.0157	0.0245
		proposed (MAP- d HMRF)	0.0009	0.0014	0.0047	0.0111
SAM [70]	NSCA	FCLS [27]	1.0034	2.7632	7.3645	11.5184
		MaxEnt [34]	2.3416	7.3678	10.7814	12.3802
		TLS-Tikhonov [31]	1.7832	11.9216	15.4017	16.1822
		MAP-HMRF [43]	2.6575	11.3154	13.3921	15.8344
		proposed (MAP- d HMRF)	0.9653	2.3421	3.9386	4.9627
	NCA	NCLS [68]	1.0003	2.8925	7.7588	12.0178
		proposed (MAP- d HMRF)	0.9942	2.6489	4.6349	5.7876
SID [71]	NSCA	FCLS [27]	0.0008	0.0129	0.0212	0.0230
		MaxEnt [34]	0.0196	0.2133	0.2912	0.3123
		TLS-Tikhonov [31]	0.0102	0.1038	0.2246	0.2528
		MAP-HMRF [43]	0.0097	0.0185	0.0989	0.1343
		proposed (MAP- d HMRF)	0.0006	0.0087	0.0118	0.0129
	NCA	NCLS [68]	0.0007	0.0153	0.0274	0.0311
		proposed (MAP- d HMRF)	0.0004	0.0096	0.0120	0.0164

NSCA: nonnegative and sum-to-one constrained abundances

NCA: nonnegative constrained abundances

While analyzing the real data, imposing the sum-to-one constraint may lead to misleading results as one may not have the complete endmember information, i.e., number of endmembers and their signatures. However, in the simulated data, we have the complete knowledge of endmembers. This prompted us to assess the performance of the proposed approach by imposing only the nonnegativity constraint on abundances. In the proposed method, only nonnegativity constraint can be imposed by choosing the candidate particles for PSO with a set of random numbers uniformly distributed between $[0, 1]$. Note that the resultant nonnegative abundance values may not necessarily be sum-to-one. Results of this experiment are compared with the nonnegative constraint least-squares (NCLS) [68] method. Unlike the proposed method which uses prior information of the abundances, the NCLS imposes only the nonnegativity constraint to obtain the solution. Hence, we expect the proposed method to perform better. The estimated abundance maps by the NCLS method and the proposed MAP- d HMRF with only nonnegativity constraint are shown in Fig. 9 at SNR = 20 dB. Fig. 9 (a) and Fig. 9 (b) show the estimated abundance maps using the NCLS and the proposed methods, respectively. One may observe from the Fig. 9 that spatial patterns of the abundances are consistent in both the methods, and the maps are also visually similar to those shown in Fig. 6. The quantitative measures with the nonnegativity constraint are shown in Table III under the NCA (nonnegative constrained abundances). From the Table III, we see that only at lowest noise level (SNR = 1000 dB), NCLS performs relatively better in terms of RMSE, however, for all other increasing levels of noise, the performance of the proposed approach is better than the NCLS [68] method.

Finally, we look at the complexity of the various approaches in terms of average processing time and it is summarized in Table IV. As far as the comparison with our previous works [31] and [43] is concerned, the proposed MAP- d HMRF approach is faster. Also it has lesser execution time than the MaxEnt approach. However, the processing time of the proposed approach is moderately higher when compared to the FCLS method. This is because of the evolutionary nature of PSO, which increases the time complexity in our method. Similarly, considering the nonnegativity constraint, the average processing time of the proposed approach is relatively higher, however, it is found in the same order as that of the NCLS method. We would like to mention here that one may use parallel implementation for decreasing the execution time using the spatial data-partitioning strategy suggested in [72] and as demonstrated in [73].

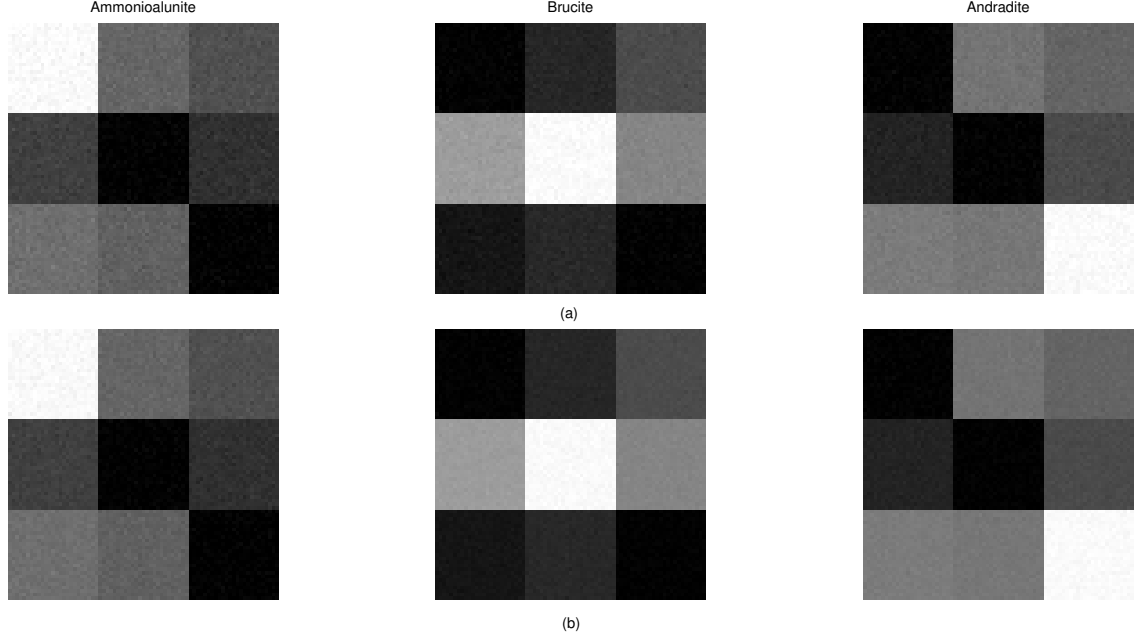


Fig. 9. Unmixed images of synthetically generated data by considering *nonnegativity constraint* only.: The results are shown for data at 20 dB SNR. Estimated abundance maps by using (a) the NCLS [68] method, and (b) the proposed MAP-dHMRF approach.

TABLE IV
AVERAGE PROCESSING TIME TO UNMIX A PIXEL LOCATION USING THE SYNTHETIC DATA OVER DIFFERENT SNR VALUES.

Algorithm	Unmixing time (in seconds)
FCLS [27]	0.0034
MaxEnt [34]	0.2543
TLS-Tikhonov [31]	0.1278
MAP-HMRF [43]	0.6835
proposed (MAP-dHMRF)	0.0331

B. Experiments on real AVIRIS data

In this subsection, we assess the effectiveness of the proposed approach on the benchmark real data. For this purpose, we consider data acquired by the AVIRIS over the Cuprite mining site [67]. The Cuprite site is rich in minerals and is located around 200 Km northwest of Las Vegas (USA). It has been extensively used in experimentation by the remote sensing research community for many years. The data is collected in 224 contiguous wavelength bands ranging from 400-2500 nm with the spectral resolution of 10 nm. For experimenting, we use only a part of the scene [74] which is located towards the east-south center of the scene. The size of an image in each band is 250×191 pixels with each pixel covering an area of $20m \times 20m$. Experiments are conducted on 188 bands after removing the bands 1-2, 104-113, 148-167 and 221-224, and they correspond to water absorption having low SNR [74]. In Fig. 10, we show one of the bands ($\#50^{th}$ spectral band) of the data since sufficient number of the minerals are visible in this band.

Based on the mineral classification maps and the information available in [75], and the published results in [14], [34], fourteen endmembers are considered within the scene of selected region. The available endmembers in this region include the following minerals, namely, Chalcedony, Alunite, Kaolinite #1, Nontronite, Kaolinite #3, Desert vanish, Dumortierite, Muscovite, Sphene, Andradite, Pyrope #1, Pyrope #2, Buddingtonite, and Montmorillonite. The virtual dimensionality (VD) [10] algorithm was also run as the verification test which also resulted in fourteen endmembers in the data.

Knowing the number of endmembers, we construct the endmember matrix using the USGS library signatures [11]. An initial estimate of the abundances was then obtained by using the matched-filters based approach which was used in deriving threshold β as was done in the case of synthetic data. In order to show the visual perception of variations of abundances, a map consist of magnitude of gradients of the initial abundance maps averaged at each pixel is displayed in Fig. 11 (a). In Fig. 11 (b) we show the histogram of these magnitudes from which a value of $\beta = 0.11$ was selected.

In general a real data may have many unidentified minerals and unknown background signatures. Hence in the absence of complete knowledge about the number of endmembers and their signatures, the unmixing results obtained using physical

constraint such as sum-to-one may lead to inaccurate estimates of abundances. Hence while using the real data we avoid the comparison of our results with the FCLS as well as the MaxEnt approaches since they impose the strict constraint on the abundances. However, we do show the comparison with the NCLS method. We also show the comparison when the NCLS output is used as the initial estimate in the proposed MAP approach. To do this, we consider the abundances estimated using the NCLS approach as an initial estimate and obtain the β as was done for the matched-filters output as the initial estimate. Fig. 12 (a) shows the image for the average magnitude of gradients of the abundances obtained using NCLS approach. In Fig. 12 (b) we show the histogram of magnitude of gradients from which $\beta = 0.15$ was derived. The final estimated abundance maps using the proposed approach are shown in Fig. 13. Due to limited space we avoid displaying estimated abundance maps using NCLS based approach and using the NCLS as an initial estimate in the MAP approach. We would like to mention here that the estimated abundance maps using the proposed method are visually closer to those of in [14], [34], [75] as well as the abundance maps estimated using the NCLS based approach and using the NCLS as an initial estimate in the MAP approach.

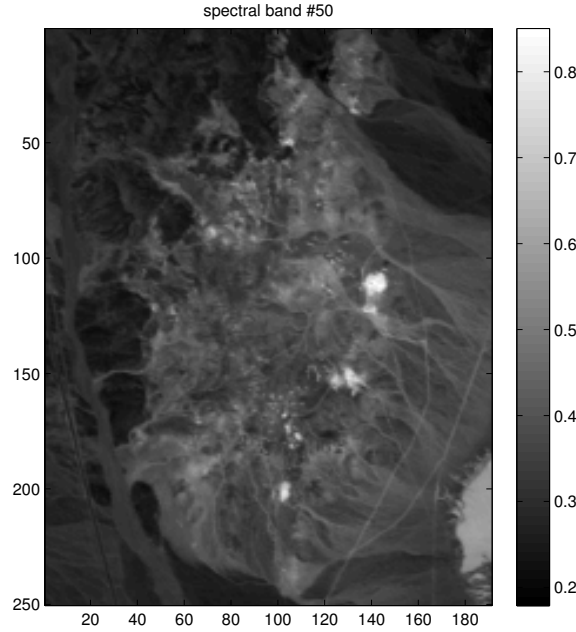


Fig. 10. The spectral band #50 of the AVIRIS Cuprite data in the selected region.

For a quantitative analysis, we first resort to reconstructing the reflectance data using the USGS endmembers while using the estimated abundances from different approaches, and measure the data reconstruction error (DRE) in terms of the RMSE at each pixel location, which is displayed as an image, i.e., a DRE map. In Fig. 14 (a) we display the DRE map for the NCLS [68] based approach. Fig. 14 (b) shows the DRE map of MAP approach using the abundances estimated using the NCLS method as the initial estimate, and in Fig. 14 (c) we display the result of the proposed MAP- d HMRf approach. It can be seen from the DRE maps that the proposed approach results in reduced mean as well as standard deviation when compared to both the NCLS as well as the MAP based on NCLS as the initial estimate, indicating lower values for reconstruction error for the proposed method. It is clear that the reduced reconstruction error is an indication of reduced unmixing error, since in these experiments we use the same endmember information for all the approaches in the comparison. One may argue that to take into account the possibility of unidentified signal sources present in the real data, it may be preferable to use the NCLS approach or use the NCLS as an initial estimate in the MAP approach when compared to the matched-filters based estimate. But as shown by the proposed approach, the value of β plays an important role in improving the accuracy of estimated abundances. The reduced error is due to the selection of proper value for β and the regularization as done in the proposed method.

In order to further quantify the results, we use the quality with no reference (QNR) [76] index from the pansharpening research [77]. It is a quality measure which does not require the availability of the ground truth abundances. Hence, it can be suitable for testing the effectiveness of the algorithms while using the real data. QNR basically generalizes the notion of universal quality index for the multi-band images [78]. We compute the QNR for the reconstructed data and assess both the spatial as well as spectral quality of the reconstructed reflectance. These measures correspond to spectral and spatial distortion indices, i.e., d_{bands} and d_{image} , respectively. QNR [76] is given by

$$QNR = (1 - d_{bands}) \cdot (1 - d_{image}). \quad (19)$$

Lower values for d_{bands} and d_{image} measures and in turn a higher value for the QNR closer to unity indicates the better data reflectance. In our case, since the endmembers are same in all the approaches, the reconstructed reflectance should differ with

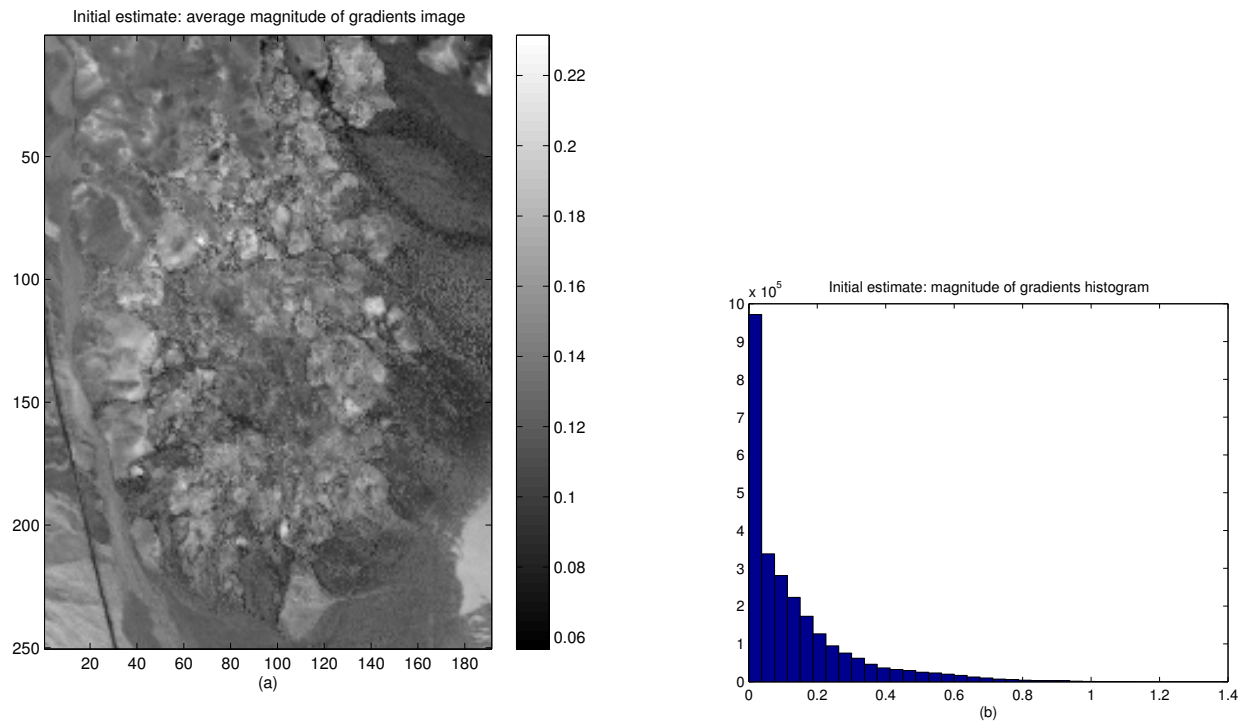


Fig. 11. Deriving data-dependent β from AVIRIS Cuprite scene using the proposed matched-filters as the initial estimate of abundances (a) average magnitude of gradients of the abundances at each location over the entire scene, and (b) histogram of magnitude of gradients of the estimated abundances. The value of $\beta = 0.11$ is selected from the histogram.

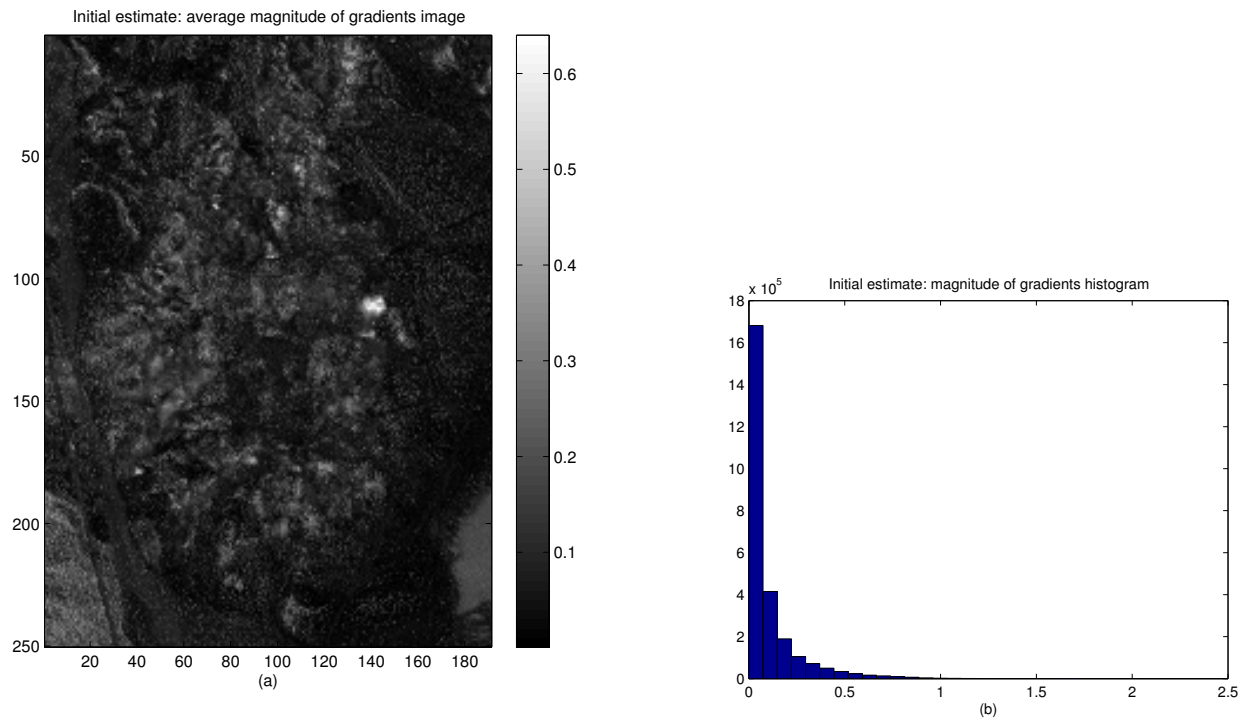


Fig. 12. Deriving data-dependent β from AVIRIS Cuprite scene using the NCLS as the initial estimate of abundances (a) average magnitude of gradients of the abundances at each location over the scene, and (b) histogram of magnitude of gradients of the estimated abundances. The value of $\beta = 0.15$ is selected from the histogram.

the different abundance estimation techniques. The d_{bands} index amounts for the inter-band distortions across the spectral range of data while the d_{image} considers the average distortions over the spatial locations. We first calculate d_{bands} and d_{image} as in [76] and then insert these values in equation (19) to compute the QNR index. Table V shows the d_{bands} , d_{image} , and QNR indices computed for the different approaches along with their ideal values. It can be seen from the table that the proposed approach has the minimum spectral and spatial indices, resulting in better QNR which indicates improved unmixing.

Finally, we carry out sensitivity analysis by reconstructing the data using the estimated abundances by varying the number of endmembers and measuring the total data reconstruction error (DRE) in each case. The total DRE is computed by summing up the DRE values at every pixel location in the DRE map. Fig. 15 shows the plot of total DRE versus number of endmembers. It can be seen from the graph that the error decreases more rapidly up to six endmembers while it is almost constant as it approaches the fourteenth endmember. After this point, the error remains almost same. We conclude that though the site has plenty of minerals and may have unidentified signal sources, these have little effect on the unmixing performance.

TABLE V
SPECTRAL DISTORTION INDEX (d_{bands}), SPATIAL DISTORTION INDEX (d_{image}) AND QUALITY-WITH-NO-REFERENCE (QNR)
OF THE RECONSTRUCTED DATA USING DIFFERENT APPROACHES.

Algorithm	d_{bands}	d_{image}	QNR
Ideal value	0.0000	0.0000	1.0000
NCLS [68]	0.2480	0.3534	0.4888
MAP with NCLS initialization	0.2261	0.3008	0.5417
proposed (MAP- d HMRF)	0.0011	0.1921	0.8091

C. Choice of PSO parameters and sensitivity analysis of λ and β

In this subsection, we discuss the choice of various PSO parameters followed by sensitivity analysis of λ and β on the final solution. In order to fix the various parameters, the experiments are conducted on the synthetic data. This gives us the flexibility in choosing the abundances over the scene and hence allows us to choose the optimum parameters based on the minimum data reconstruction error for different levels of noise in the data. We select the synthetic data as reference to carry out the sensitivity analysis for λ and β . The same parameters are used while conducting the experiments on the real data.

Being an evolutionary algorithm, the parameter settings of PSO are to be done based on the problem at hand. PSO works by moving the swarm of particles, i.e., possible solutions, in the search space with improvements in search influenced by the other particles. Hence the optimization by PSO is dependent on the swarm size and initialization of particles. Though the use of larger swarm size speed-up the convergence, it happens at the cost of increased computations [79]–[81]. As a compromise, we choose nine particles and they include the abundances obtained using the FCLS, matched-filters and abundances drawn from Dirichlet distribution. By doing so we restrict the solution space that achieves faster convergence. The PSO expression given in equation (13) has three parameters, c_1 , c_2 , and w , which have to be chosen carefully for better convergence. Researchers have studied the behavior of these parameters on the solution by using a set of standard functions for minimization and have recommended using low values for c_1 and c_2 [79]–[81]. We tested the performance of PSO algorithm on the synthetic data by choosing various low values of c_1 , c_2 , and w , and finally set $c_1 = c_2 = 0.01$, and $w = 0.01$ that resulted in quick convergence.

We now demonstrate the sensitivity of λ as well as β on the solution obtained by varying each of them independently [82]. This provides an opportunity to test the effect of individual parameter on the solution. By selecting the derived value of β and conducting experiments using different λ values, we found that the performance of our approach was optimum when the data and the prior terms have equal weightage, i.e., $\lambda = 1$. The RMSE maps for three different values of λ at the highest noise level of SNR = 20dB is shown in Fig. 16. One can observe from the RMSE maps that the use of $\lambda = 1$ reduces the average error and has lower standard deviation. We reiterate here that one may use the generalized cross validation (GCV) technique and estimate the regularization parameter λ . However GCV is computationally expensive and we refrain from doing the same in our approach.

A proper value of β is very important as far as the performance of the proposed approach is concerned. β is a global threshold that characterizes the variations of the abundances across the acquired scene. In order to obtain the correct value for the β , one must have the true abundances which are not available, as they are to be estimated. Due to the nonavailability of the strong mathematical models, one has to look for solving such practical problems by using the available data itself. To this end, one can use initial estimate of abundances that preserves the statistical characteristics of abundances. As discussed in section IV, the matched-filters based approach enhances the signal-to-noise ratio (SNR) of the output by considering the properties of data covariance that characterizes the needed global behavior of abundances. Hence we choose the matched-filters based approach in order to derive the initial estimate in the proposed approach.

Now, we verify the suitability of using Huber threshold β estimated from matched-filters in the proposed approach by conducting the experiments on the synthetic data. The experiments are also conducted by using the β derived from the FCLS and MaxEnt approaches, including the empirically selected β as in MAP-HMRF [43]. Since the NCLS based approach was performing poor, we avoid considering the NCLS as an initial estimate. Fig. 17 shows the sensitivity of the proposed approach

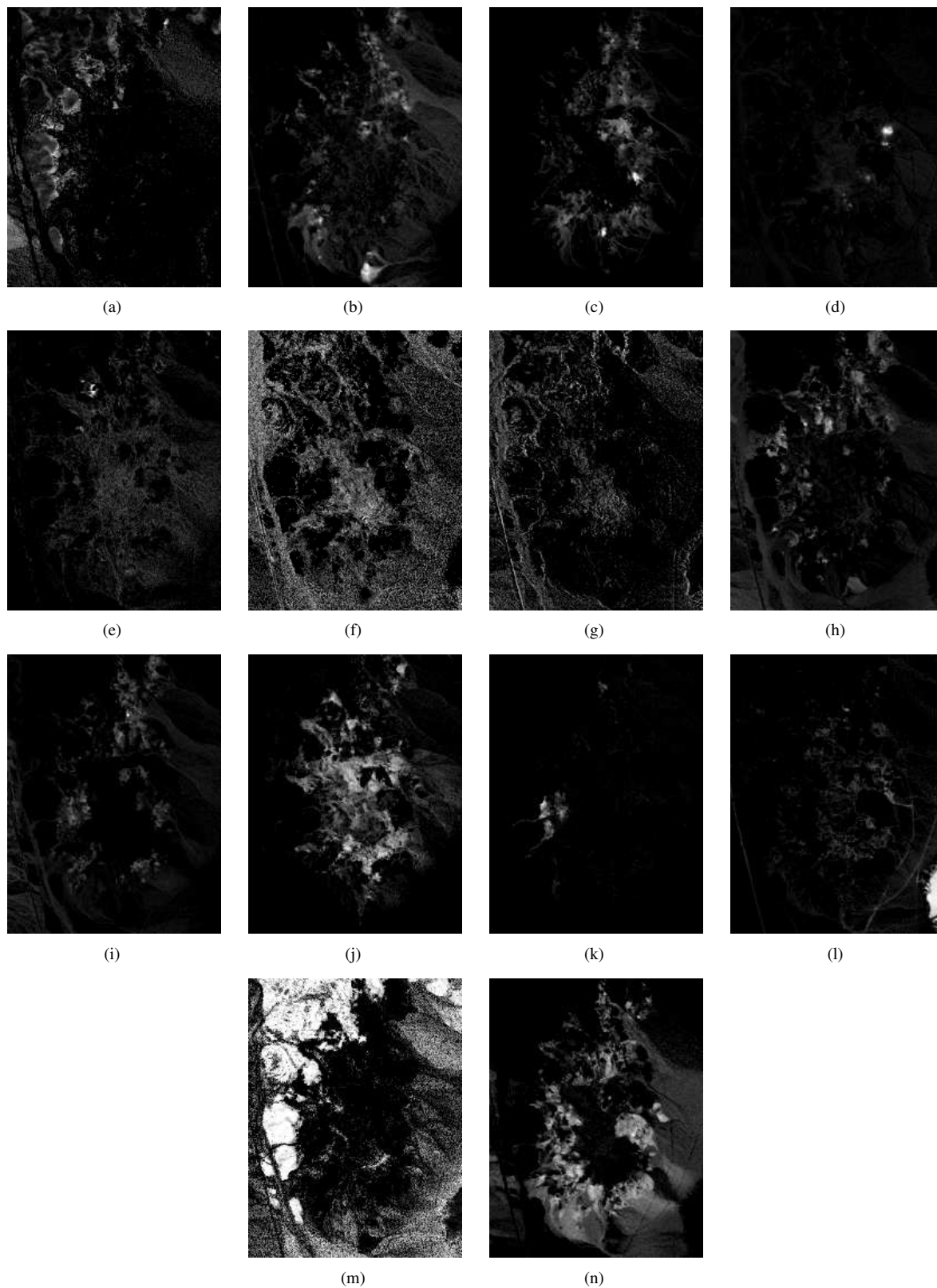


Fig. 13. Abundance maps estimated using the proposed MAP- d HMMRF approach for the Cuprite scene. (a) Pyrope #1 (b) Kaolinite #3 (c) Pyrope #2 (d) Muscovite (e) Nontronite (f) Desert vanish (g) Andradite (h) Dumortierite (i) Kaolinite #1 (j) Chalcedony (k) Buddingtonite (l) Montmorillonite (m) Sphene and (n) Alunite.

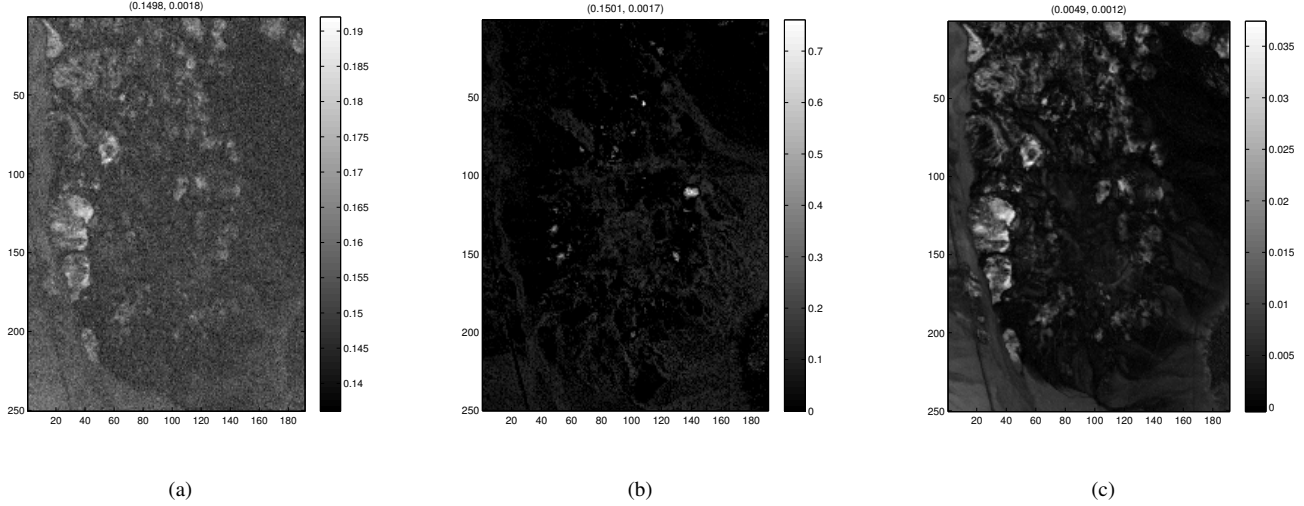


Fig. 14. Data reconstruction error (DRE) maps for AVIRIS Cuprite scene. (a) using NCLS [68] based approach, (b) MAP with the NCLS as an initial estimate, and (c) proposed MAP-dHMRF approach with nonnegativity constraint. The average errors and their standard deviations are mentioned in parenthesis on the top of each figure. Since the endmember information remains same in all the three cases, the variance of the error is an indication of the difference in estimated abundances by the different approaches. It can be seen that the proposed approach is better in terms of RMSE as well as preservation of abundances variance.

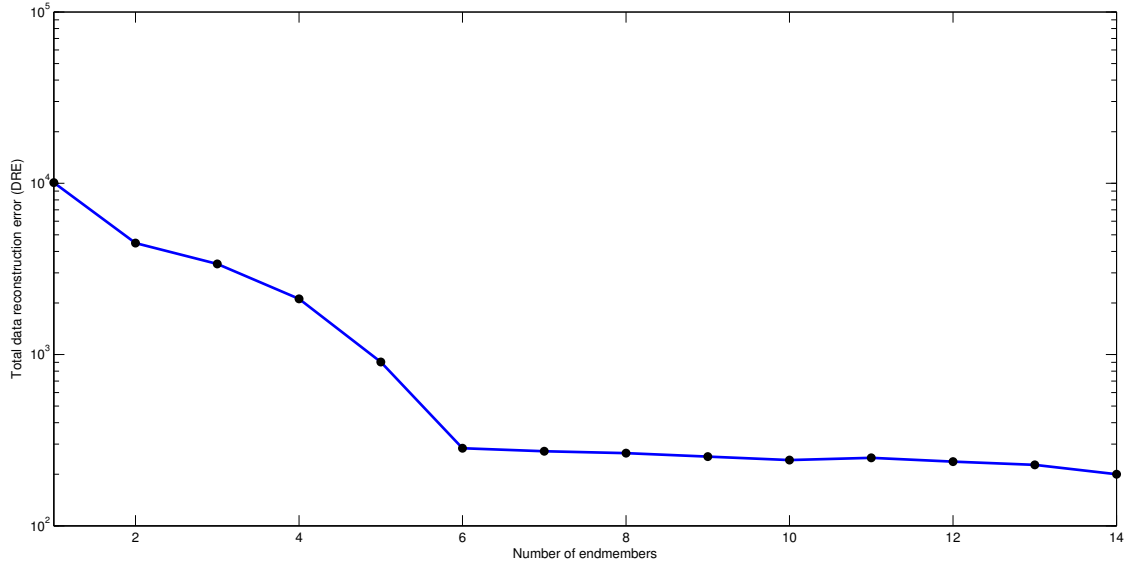


Fig. 15. Total data reconstruction error for increasing number of endmembers in the AVIRIS Cuprite scene.

in terms of RMSE. Though the values of β obtained using different approaches are same at lowest noise level (i.e., almost no noise in the data), there exist difference with the increasing noise levels. The empirically set β as in the MAP-HMRF case does not guarantee minimum reconstruction error as seen from Fig. 17 (g-i). One can see that the MAP solution with the β derived using the FCLS as well as MaxEnt approaches do not yield better solution as indicated by the higher RMSE in the Fig. 17 (b), Fig. 17 (c), Fig. 17 (e), and Fig. 17 (f). This is because the increase in noise affects the LS solution and hence the derived β is inaccurate. By comparing the RMSE maps displayed in Fig. 17, one can observe significant reduction in the average errors as well as the standard deviations for the β obtained using the matched-filters as done in our proposed MAP-dHMRF approach (see Fig. 17 (k) and Fig. 17 (l)).

VIII. CONCLUSIONS AND FUTURE RESEARCH

We have presented a novel approach for unmixing which overcomes the ill-posedness due to the noise and outliers in the data, ill-conditioning of endmember matrix as well as preserves the sudden variations in abundances. It has an MAP solution with the data-dependent Huber-MRF prior across the contiguous spectral measurements of the scene. Huber threshold β is

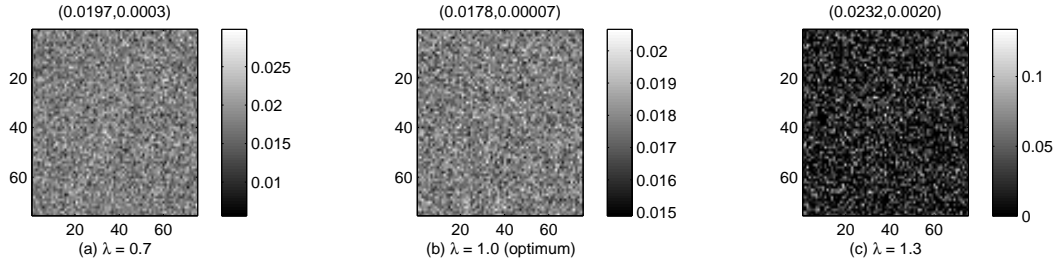


Fig. 16. RMSE maps for the MAP approach using different values of λ at 20 dB SNR in the synthetic data. RMSE map for (a) $\lambda = 0.7$, (b) $\lambda = 1.0$, and (c) for $\lambda = 1.3$. The average errors and their standard deviations are mentioned in the parenthesis on the top of each figure. We see that the RMSE and standard deviation are minimum for $\lambda = 1$.

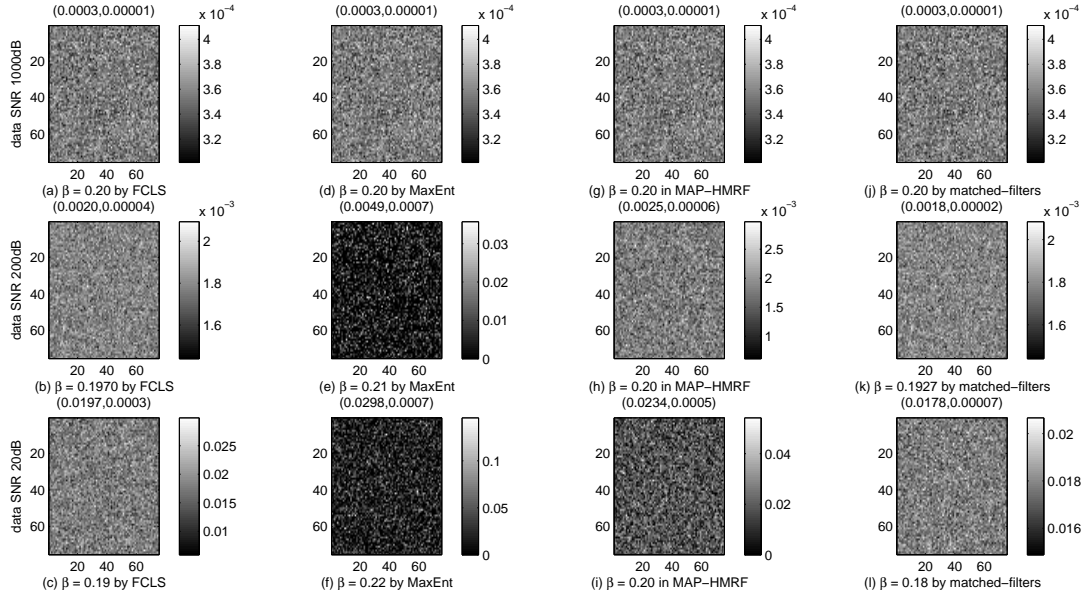


Fig. 17. RMSE maps: Sensitivity analysis for MAP solution using β derived from various initial estimates with increasing noise levels (SNR = 1000 dB, 200 dB, and 20 dB) in the synthetic data. RMSE maps (a-c) for β obtained using the FCLS as initial estimate, (d-f) for β derived using MaxEnt, (g-i) for empirical value of β as used in MAP-HMRF, and (j-l) for β as obtained using the matched filters as the initial estimate (i.e., proposed MAP-dHMRF). The average errors and their standard deviations are mentioned in parenthesis on the top of each figure. We see that the better estimate of β obtained by using the matched-filters ensures the minimum average errors and drastic reduction in standard deviations which in turn results in preserving the variance in abundances.

derived from the initial estimate of abundances which is found using the matched filters based approach for the endmembers. The detail theoretical analysis shows that the proposed two-step Bayesian approach obtains abundances that minimize the reconstruction error and the experimental demonstration validates the effectiveness of the proposed solution. Deriving the β from the given data obviates the training data resources and the subsequent learning process. Our future work involves the parallel implementation of the algorithm on graphical processing unit (GPU). This is particularly useful while porting for the high performance computing based applications of the hyperspectral data.

ACKNOWLEDGMENT

Authors would like to thank the associate editor and the three anonymous reviewers for their insightful comments and suggestions which we believe has greatly improved the clarity as well as the quality of the paper. Thanks to Prof. Antonio Plaza, University of Extremadura, Spain for providing us the synthetic data with ground truth information. The authors also acknowledge the United States Geological Survey (USGS) for the publicly available spectral library of minerals, datasets and their mineral maps.

REFERENCES

- [1] A. F. H. Goetz and et. al., "Imaging spectrometry for earth remote sensing," *Science*, vol. 228, no. 4704, pp. 1147–1153, 1985.
- [2] R. O. Green, M. L. Eastwood, C. M. Sarture, T. G. Chrien, M. Aronsson, B. J. Chippendale, J. A. Faust, B. E. Pavri, C. J. Chovit, M. Solis, and et al., "Imaging spectroscopy and the airborne visible infrared imaging spectrometer (aviris)," *Remote Sensing of Environment*, vol. 65, no. 3, pp. 227–248, 1998.

- [3] J. Boardman, "Analysis, understanding and visualization of hyperspectral data as convex sets in n-space," *Proc. SPIE Imaging Spectrometry*, vol. 2480, pp. 23–36, 1995.
- [4] A. D. Stocker and A. P. Schaum, "Application of stochastic mixing models to hyperspectral detection problems," *Proc. SPIE*, vol. 3071, pp. 47–60, 1997.
- [5] M. T. Eismann and R. C. Hardie, "Initialization and convergence of the stochastic mixing model," *Proc. SPIE, Imaging Spectrometry IX*, vol. 5159, pp. 307–318, 2003.
- [6] C.-I. Chang, Ed., *Hyperspectral Data Exploitation: Theory and Applications*. Wiley-Interscience, John Wiley & Sons, pp. 107–148, 2007.
- [7] J. Bioucas-Dias, A. Plaza, N. Dobigeon, M. Parente, Q. Du, P. Gader, and J. Chanussot, "Hyperspectral unmixing overview: Geometrical, statistical, and sparse regression-based approaches," *IEEE Journal of Selected Topics in Applied Earth Observations and Remote Sensing*, vol. 5, no. 2, pp. 354–379, 2012.
- [8] A. Plaza, J. A. Benediktsson, J. W. Boardman, J. Brazile, L. Bruzzone, G. Camps-Valls, J. Chanussot, M. Fauvel, P. Gamba, A. Gualtieri, and et al., "Recent advances in techniques for hyperspectral image processing," *Remote Sensing of Environment*, vol. 113, no. Supplement 1, pp. S110–S122, 2009.
- [9] A. Plaza, G. Mart, J. Plaza, M. Zortea, and S. Sergio, "Recent developments in endmember extraction and spectral unmixing," *Optical Remote Sensing Advances in Signal Processing and Exploitation Techniques*, pp. 1–33, 2010.
- [10] C.-I. Chang and Q. Du, "Estimation of number of spectrally distinct signal sources in hyperspectral imagery," *IEEE Transactions on Geoscience and Remote Sensing*, vol. 42, no. 3, pp. 608–619, 2004.
- [11] [Online]. Available: <http://speclab.cr.usgs.gov/spectral-lib.html>
- [12] J. Boardman, "Automating spectral unmixing of aviris data using convex geometry concepts," in *Summaries of 4th annual JPL Airborne Geoscience Workshop*, vol. 1, pp. 11–14, 1993.
- [13] M. E. Winter, "N-findr: an algorithm for fast autonomous spectral end-member determination in hyperspectral data," in *Proc. SPIE Image Spectrometry V*, Vol. 3753, pp. 266–277, 1999.
- [14] J. Nascimento and J. Dias, "Vertex component analysis: a fast algorithm to unmix hyperspectral data," *IEEE Transactions on Geoscience and Remote Sensing*, vol. 43, no. 4, pp. 898–910, 2005.
- [15] C.-I. Chang, C.-C. Wu, and H.-M. Chen, "Random pixel purity index," *IEEE Geoscience and Remote Sensing Letters*, vol. 7, no. 2, pp. 324–328, april 2010.
- [16] A. Plaza, P. Martinez, R. Perez, and J. Plaza, "Spatial/spectral endmember extraction by multidimensional morphological operations," *IEEE Transactions on Geoscience and Remote Sensing*, vol. 40, no. 9, pp. 2025–2041, 2002.
- [17] D. Rogge, B. Rivard, J. Zhang, A. Sanchez, J. Harris, and J. Feng, "Integration of spatial-spectral information for the improved extraction of endmembers," *Remote Sensing of Environment*, vol. 110, no. 3, pp. 287–303, 2007.
- [18] M. Zortea and A. Plaza, "Spatial preprocessing for endmember extraction," *IEEE Transactions on Geoscience and Remote Sensing*, vol. 47, pp. 2679–2693, 2009.
- [19] G. Martin and A. Plaza, "Spatial-spectral preprocessing prior to endmember identification and unmixing of remotely sensed hyperspectral data," *IEEE Journal of Selected Topics in Applied Earth Observations and Remote Sensing*, vol. 5, no. 2, pp. 380–395, 2012.
- [20] C.-I. Chang, *Hyperspectral imaging: Techniques for Spectral Detection and Classification*. New York: Kluwer Academic/Plenum Publishers, 2003.
- [21] L. Parra, K.-R. Mueller, C. Spence, A. Ziehe, and P. Sajda, "Unmixing hyperspectral data," *Proc. Advanced Neural Information Processes Systems (NIPS)*, vol. 12, pp. 942–948, 2000.
- [22] N. Keshava, "A survey of spectral unmixing algorithms," *Lincoln Laboratory Journal*, vol. 14, no. 1, pp. 55–78, 2003.
- [23] P. Masson and W. Pieczynski, "Sem algorithm and unsupervised statistical segmentation of satellite images," *IEEE Transactions on Geoscience and Remote Sensing*, vol. 31, no. 3, pp. 618–633, 1993.
- [24] S. Mei, M. He, Z. Wang, and D. Feng, "Mixture analysis by multichannel hopfield neural network," *IEEE Geoscience and Remote Sensing Letters*, vol. 7, no. 3, pp. 455–459, 2010.
- [25] A. Barducci and A. Mecocci, "Theoretical and experimental assessment of noise effects on least-squares spectral unmixing of hyperspectral images," *Optical Engineering*, vol. 44, pp. 100–108, 2005.
- [26] J. Settle, "On the effect of variable endmember spectra in the linear mixture model," *IEEE Transactions on Geoscience and Remote Sensing*, vol. 44, pp. 389–396, 2006.
- [27] D. Heinz and C.-I. Chang, "Fully constrained least squares linear spectral mixture analysis method for material quantification in hyperspectral imagery," *IEEE Transactions on Geoscience and Remote Sensing*, vol. 39, no. 3, pp. 529–545, 2001.
- [28] M. T. Eismann and R. C. Hardie, "Stochastic spectral unmixing with enhanced endmember class separation," *Applied Optics*, vol. 43, no. 36, pp. 6596–6608, 2004.
- [29] Y. Hu, H. Lee, and F. Scarpace, "Optimal linear spectral unmixing," *IEEE Transactions on Geoscience and Remote Sensing*, vol. 37, pp. 639–644, 1999.
- [30] B. Sirkeci, D. Brady, and J. Burman, "Restricted total least squares solutions for hyperspectral imagery," in *IEEE International Conference on Acoustics, Speech, and Signal Processing, ICASSP '00 Proc.*, vol. 1, 2000, pp. 624–627.
- [31] J. S. Bhatt, M. V. Joshi, and M. S. Raval, "A regularization based method for spectral unmixing of imaging spectrometer data," *Proc. SPIE, Image and Signal Processing for Remote Sensing XVIII*, vol. 8537, pp. 85370J1–7, 2012.
- [32] S. Chettri and N. S. Netanyahu, "Spectral unmixing of remotely sensed imagery using maximum entropy," in *Proc. SPIE*, 1997.
- [33] L. Miao, H. Qi, and H. Szu, "Unsupervised decomposition of mixed pixels using the maximum entropy principle," in *18th International Conference on Pattern Recognition, ICPR 2006.*, vol. 1, 2006, pp. 1067–1070.
- [34] —, "A maximum entropy approach to unsupervised mixed-pixel decomposition," *IEEE Transactions on Image Processing*, vol. 16, no. 4, pp. 1008–1021, 2007.
- [35] S. Moussaoui, C. Carteret, C. Brie, and A. Mohammad-Djafari, "Bayesian analysis of spectral mixture data using markov chain monte carlo methods," *Chemometrics and Intelligent Laboratory Systems*, vol. 81, no. 2, pp. 137–148, 2006.
- [36] N. Dobigeon, S. Moussaoui, J.-Y. Tourneret, and C. Carteret, "Bayesian separation of spectral sources under non-negativity and full additivity constraints," *Signal Processing*, vol. 89, no. 12, pp. 2657–2669, 2009.
- [37] N. Dobigeon, S. Moussaoui, M. Coulon, J.-Y. Tourneret, and A. Hero, "Joint bayesian endmember extraction and linear unmixing for hyperspectral imagery," *IEEE Transactions on Signal Processing*, vol. 57, no. 11, pp. 4355–4368, 2009.
- [38] F. Schmidt, A. Schmidt, E. Treguier, M. Guiheneuf, S. Moussaoui, and N. Dobigeon, "Implementation strategies for hyperspectral unmixing using bayesian source separation," *IEEE Transactions on Geoscience and Remote Sensing*, vol. 48, no. 11, pp. 4000–4013, 2010.
- [39] M. Arngren, M. Schmidt, and J. Larsen, "Unmixing of hyperspectral images using bayesian nonnegative matrix factorization with volume prior," *Journal of Signal Processing Systems*, vol. 65, no. 3, pp. 479–496, 2011.
- [40] J. Kent and K. Mardia, "Spatial classification using fuzzy membership models," *IEEE Transactions on Pattern Analysis and Machine Intelligence*, vol. 10, no. 5, pp. 659–671, 1988.
- [41] R. Rand and D. Keenan, "A spectral mixture process conditioned by gibbs-based partitioning," *IEEE Transactions on Geoscience and Remote Sensing*, vol. 39, no. 7, pp. 1421–1434, 2001.
- [42] O. Eches, N. Dobigeon, and J.-Y. Tourneret, "Enhancing hyperspectral image unmixing with spatial correlations," *IEEE Transactions on Geoscience and Remote Sensing*, vol. 49, no. 11, pp. 4239–4247, 2011.
- [43] J. S. Bhatt, M. V. Joshi, and M. S. Raval, "A parametric statistical model over spectral space for the unmixing of imaging spectrometer data," *Proc. SPIE, Image and Signal Processing for Remote Sensing XVIII*, vol. 8537, pp. 85371J1–7, 2012.

- [44] P. J. Huber, "Robust estimation of a location parameter," *The Annals of Mathematical Statistics*, vol. 35, no. 1, pp. 73–101, 1964.
- [45] D. O. North, "An analysis of the factors which determine signal/noise discrimination in pulsed carrier systems," *Proc. IEEE*, vol. 51, no. 7, pp. 1016–1027, 1963.
- [46] J. Chen and I. Reed, "A detection algorithm for optical targets in clutter," *IEEE Transactions on Aerospace and Electronic Systems*, vol. AES-23, no. 1, pp. 46–59, 1987.
- [47] J. Harsanyi and C.-I. Chang, "Hyperspectral image classification and dimensionality reduction: an orthogonal subspace projection approach," *IEEE Transactions on Geoscience and Remote Sensing*, vol. 32, no. 4, pp. 779–785, 1994.
- [48] A. P. Schaum and A. D. Stocker, "Subpixel detection methods: spectral unmixing, correlation processing and when they are appropriate," in *Proc. of International Symposium on Spectral Sensing Research*, 1994.
- [49] B. Shahraray and D. Anderson, "Optimal estimation of contour properties by cross-validated regularization," *IEEE Transactions on Pattern Analysis and Machine Intelligence*, vol. 11, no. 6, pp. 600–610, 1989.
- [50] I. Dopido, A. Villa, A. Plaza, and P. Gamba, "A quantitative and comparative assessment of unmixing-based feature extraction techniques for hyperspectral image classification," *IEEE Journal of Selected Topics in Applied Earth Observations and Remote Sensing*, vol. 5, no. 2, pp. 421–435, april 2012.
- [51] A. J. Plaza, "Content-based hyperspectral image retrieval using spectral unmixing," *Proc. SPIE 8180, Image and Signal Processing for Remote Sensing XVII*, 81800O, pp. 81 800O1–8, 2011.
- [52] M. A. Veganzones and M. Grana, "A spectral/spatial cbir system for hyperspectral images," *IEEE Journal of Selected Topics in Applied Earth Observations and Remote Sensing*, vol. 5, no. 2, pp. 488–500, 2012.
- [53] A. Plaza, P. Martinez, R. Perez, and J. Plaza, "A new method for target detection in hyperspectral imagery based on extended morphological profiles," in *IEEE IGARSS Symposium*, 2003.
- [54] C. Yang, J. H. Everitt, and Q. Du, "Applying linear spectral unmixing to airborne hyperspectral imagery for mapping yield variability in grain sorghum and cotton fields," *SPIE Journal of Applied Remote Sensing*, vol. 4, p. 041887, 2010.
- [55] G. Licciardi, A. Villa, M. Khan, and J. Chanussot, "Image fusion and spectral unmixing of hyperspectral images for spatial improvement of classification maps," in *IEEE IGARSS Symposium*, pp. 7290–7293, 2012.
- [56] S. Dowler and M. Andrews, "Abundance guided endmember selection: An algorithm for unmixing hyperspectral data," *17th IEEE International Conference on Image Processing (ICIP 2010)*, pp. 2649–2652, 2010.
- [57] T. P. Minka, "Estimating a dirichlet distribution," M.I.T., Tech. Rep., 2000, revised 2003, 2009.
- [58] J. W. Boardman and F. A. Kruse, "Analysis of imaging spectrometer data using n-dimensional geometry and a mixture-tuned matched filtering approach," *IEEE Transactions on Geoscience and Remote Sensing*, vol. 49, no. 11, pp. 4138–4152, 2011.
- [59] P. C. Mahalanobis, "On the generalised distance in statistics," *In Proceedings of the National Institute of Sciences of India*, vol. 2, pp. 49–55, 1936.
- [60] J. Kennedy and R. Eberhart, "Particle swarm optimization," *In Proc. of IEEE International Conference on Neural Networks*, vol. 4, pp. 1942–1948, 1995.
- [61] B. Zhang, X. Sun, L. Gao, and L. Yang, "Endmember extraction of hyperspectral remote sensing images based on the discrete particle swarm optimization algorithm," *IEEE Transactions on Geoscience and Remote Sensing*, vol. 49, no. 11, pp. 4173–4176, 2011.
- [62] H. Yang, Q. Du, and G. Chen, "Particle swarm optimization-based hyperspectral dimensionality reduction for urban land cover classification," *IEEE Journal of Selected Topics in Applied Earth Observations and Remote Sensing*, vol. 5, no. 2, pp. 544–554, april 2012.
- [63] A. Zare and P. Gader, "Endmember detection using the dirichlet process," in *19th International Conference on Pattern Recognition, ICPR*, 2008, pp. 1–4.
- [64] J. M. Nascimento and J. M. Bioucas-Dias, "Nonlinear mixture model for hyperspectral unmixing," *Proc. SPIE 7477, Image and Signal Processing for Remote Sensing XV*, 7477OI, pp. 7477OI1–8, 2009.
- [65] J. M. Bioucas-Dias and J. Nascimento, "Hyperspectral unmixing based on mixtures of dirichlet components," *IEEE Transactions on Geoscience and Remote Sensing*, vol. 50, no. 3, pp. 863–878, 2012.
- [66] R. Bro and S. Jong, "A fast non-negativity constrained least squares algorithm," *Journal of Chemometrics*, vol. 11, pp. 393–401, 1997.
- [67] [Online]. Available: http://aviris.jpl.nasa.gov/data/free_data.html
- [68] C. L. Lawson and R. J. Hanson, *Solving Least Squares Problems*. SIAM, 1995.
- [69] Z. Wang and A. C. Bovik, "Mean squared error: Love it or leave it? a new look at signal fidelity measures," *IEEE Signal Processing Magazine*, vol. 26, pp. 98–117, 2009.
- [70] R. Yuhans, A. Goetz, and J. Boardman, "Discrimination among semi-arid landscape endmembers using the spectral angle mapper (sam) algorithm," in *Proc. Summaries 3rd Annu. JPL Airborne Geoscience Workshop, R.O. Green, Ed.*, vol. 1, 1992, pp. 147–149.
- [71] C.-I. Chang, "An information-theoretic approach to spectral variability, similarity, and discrimination for hyperspectral image analysis," *IEEE Transactions on Information Theory*, vol. 46, no. 5, pp. 1927–1932, 2000.
- [72] A. Plaza, J. Plaza, A. Paz, and S. Sanchez, "Parallel hyperspectral image and signal processing," *IEEE Signal Processing Magazine*, vol. 28, no. 3, pp. 119–126, 2011.
- [73] A. Plaza and J. Plaza, "Parallel implementation of linear and nonlinear spectral unmixing of remotely sensed hyperspectral images," *Proc. SPIE 8183, High-Performance Computing in Remote Sensing*, 81830D, 2011.
- [74] [Online]. Available: http://www.lx.it.pt/~bioucas/code/unmixing_overview.zip
- [75] G. Swayze, "The hydrothermal and structural history of the cuprite mining district, southwestern nevada: An integrated geological and geophysical approach," Ph.D. dissertation, University of Colorado, Boulder, 1997.
- [76] L. Alparone, B. Alazzi, S. Barnoti, A. Garzelli, F. Nencini, and M. Selva, "Multispectral and panchromatic data fusion assessment without reference," *Photogrammetric Engineering and Remote Sensing*, vol. 74, no. 2, pp. 193–200, 2008.
- [77] M. Khan, J. Chanussot, and L. Alparone, "Hyperspectral pansharpening using qnr optimization constraint," *Hyperspectral Image and Signal Processing: Evolution in Remote Sensing (WHISPERS)*, pp. 1–4, 2009.
- [78] Z. Wang and A. C. Bovik, "A universal image quality index," *IEEE Signal Processing Letters*, vol. 9, no. 3, pp. 81–84, 2002.
- [79] I. C. Trelea, "The particle swarm optimization algorithm: convergence analysis and parameter selection," *Information Processing Letters*, vol. 85, no. 6, pp. 317–325, 2003.
- [80] L.-P. Zhang, H.-J. Yu, and S.-X. Hu, "Optimal choice of parameters for particle swarm optimization," *Journal of Zhejiang University Science A*, vol. 6, no. 6, pp. 528–534, 2005.
- [81] M. E. H. Pedersen, "Good parameters for particle swarm optimization," Hvass Laboratory, Copenhagen, Denmark, Tech. Rep., 2010.
- [82] D. Hamby, "A review of techniques for parameter sensitivity analysis of environment models," *Environmental Monitoring and Assessment*, vol. 32, no. 2, pp. 135–154, 1994.



Jignesh S. Bhatt was born in Bhavnagar, Gujarat, India. He obtained his BE in Electronics & Communications (2000) from North Gujarat University and MTech in Communication Systems (2008) from SVNIT, India. He served as Assistant Professor for over 8 years in Gujarat, India. Since the year 2009, he is full-time PhD research scholar in Information and Communication Technology (ICT) at DA-IICT, Gandhinagar, India. His research interests focus on signal processing for remote sensing data, multispectral and hyperspectral image analysis, estimation and applications. During the year 2007-08, he has contributed in the Space mission by developing algorithms and operational software for automatic data registration for the images from payloads INSAT-3A and KALPANA-1 used for meteorological predictions. He has generated the reference boundaries for CCD images from the INSTA-3A and being used in the Navigation program at ISRO (India). He has also carried out project at BISAG-DST (India) during the year 1999-2000. He has publications in peer-reviewed National and International conferences including SPIE. He is a student member of IEEE, a life member of ISTE (India) and an associate member of IEI (India).



Manjunath V. Joshi was born in Ranebennur, Karnataka, India. He obtained his BE degree from Mysore University and MTech and PhD degrees from IIT Mumbai, India. At present he is serving as Professor at Dhirubhai Ambani Institute of Information and Communication Technology (DA-IICT), Gandhinagar, India. He has been involved in active research in the areas of signal processing, image processing and computer vision for the last eight years. He has co-authored a book entitled Motion- Free Super Resolution published by Springer, New- York. He was given the outstanding researcher award in Engineering Section by Research Scholars Forum of IIT Bombay, India. He also received the Best PhD Thesis Award by Infineon India. He received the Dr. Vikram Sarabhai Award for the year 2006-07 in the field of Information Technology constituted by the Government of Gujarat, India. He serves as a reviewer for many of the International Conferences/Journals in his areas of expertise. He is a member of IEEE and a life member of IETE (India).



Mehul S. Raval received his Bachelor in Electronics & Telecommunication Engineering (1996) and Master of Engineering in Digital Systems (2002) from Government College of Engineering, Pune, popularly known as COEP. He received PhD in Electronics & Telecommunication Engineering from Pune University, India in 2008. Currently he is an Associate Professor at Institute of Information and Communication Technology (IICT), Ahmedabad University, India. His research interests are in the area of image processing, computer vision, digital watermarking, hyperspectral image analysis and digital image forensics. He is investigating sponsored projects for Department of Atomic energy, Govt. of India in the domain of data hiding and robust face recognition. He is recipient of many awards including best engineering teacher award for the state of Gujarat in 2005. He is an active member of many professional organizations and currently he is vice chair IEEE Gujarat section.